Geochemistry Geophysics Geosystems G3

Article
Volume 15, Number 1
22 January 2014
doi: 10.1002/2013GC005022
ISSN: 1525-2027

Published by AGU and the Geochemical Society

A systematic 2-D investigation into the mantle wedge's transient flow regime and thermal structure: Complexities arising from a hydrated rheology and thermal buoyancy

G. Le Voci
Department of Earth Science and Engineering, Imperial College London, London, UK

D. R. Davies
Department of Earth Science and Engineering, Imperial College London, London, UK

Research School of Earth Sciences, Australian National University, Mills Road, Acton, Canberra, Australian Capital Territory 0200, Australia (rhodri.davies@anu.edu.au)

S. Goes and S. C. Kramer
Department of Earth Science and Engineering, Imperial College London, London, UK

C. R. Wilson
Lamont-Doherty Earth Observatory, Columbia University, Palisades, New York, USA

[1] Arc volcanism at subduction zones is likely regulated by the mantle wedge's flow regime and thermal structure and, hence, numerous studies have attempted to quantify the principal controls on mantle wedge conditions. In this paper, we build on these previous studies by undertaking a systematic 2-D numerical investigation into how a hydrated rheology and thermal buoyancy influence the wedge's flow regime and associated thermal structure. We quantify the role of a range of plausible: (i) water contents (0–5000 H/10^{6}Si); (ii) subduction velocities (2–10 cm/yr); and (iii) upper-plate ages (50–120 Myr), finding that small-scale convection (SSC), resulting from Rayleigh-Taylor instabilities, or drips, off the base of the overriding lithosphere, is a typical occurrence. The morphology of SSC varies with viscosity and subduction parameters, with drips at their most prominent when subduction velocities and wedge viscosities are low. Our results confirm that high subduction velocities and wedge viscosities promote a dominantly corner-flow regime, and strong upper-plate erosion below the arc region. By contrast, we find that back-arc upper-plate erosion by SSC is largely controlled by wedge viscosity, occurring when: (i) viscosities are $< 5{\cdot}10^{18}$ Pa s; and (ii) the length of the upper plate, available for destabilization, exceeds the characteristic wavelength of instabilities. Thus, if hydrous weakening of wedge rheology extends at least 100–150 km from the trench, our 2-D models predict an unstable flow regime, resulting in temperature fluctuations of 50–100 K, which are sufficient to influence melting and the stability of hydrous minerals.

Components: 22,594 words, 11 figures, 2 tables.

Keywords: subduction; mantle wedge; arc volcanism; small-scale convection; rheology; melting.

Index Terms: 8170 Subduction zone processes: Tectonophysics; 8162 Rheology: mantle: Tectonophysics; 1031 Subduction zone processes: Geochemistry; 3060 Subduction zone processes: Marine Geology and Geophysics; 3613 Subduction zone processes: Mineralogy and Petrology; 8413 Subduction zone processes: Volcanology; 8033 Rheology: mantle: Structural Geology; 0545 Modeling: Computational Geophysics; 1952 Modeling: Informatics; 4255 Numerical modeling: Oceanography: General; 4316 Physical modeling: Natural Hazards.

Received 4 September 2013; **Revised** 26 November 2013; **Accepted** 26 November 2013; **Published** 22 January 2014.

Le Voci, G., D. R. Davies, S. Goes, S. C. Kramer, and C. R. Wilson (2014), A systematic 2-D investigation into the mantle wedge's transient flow regime and thermal structure: Complexities arising from a hydrated rheology and thermal buoyancy, *Geochem. Geophys. Geosyst.*, *15*, 28–51, doi:10.1002/2013GC005022.

1. Introduction

[2] Subduction zones are host to the largest earthquakes and most violent volcanic eruptions recorded on Earth. The magmatic processes occurring in these regions play a fundamental role in Earth's long-term thermochemical evolution, including the formation and growth of continental crust [e.g., *McCulloch and Bennett*, 1994; *Hawkesworth et al*., 2010]. The mantle wedge, which is bounded by the downgoing and overriding plates, plays an important role in the integrated subduction system, controlling the partitioning of fluids into the deep mantle and toward the upper plate, where they control arc volcanism [e.g., *Tatsumi*, 1989; *Manning*, 2004]. It is likely that the mantle wedge also plays a crucial role in the dynamics of subduction, influencing the extent of coupling between the downgoing plate and the overlying mantle [e.g., *Billen and Gurnis*, 2001; *Manea and Gurnis*, 2007]. An improved understanding of the subduction zone mantle wedge is therefore of fundamental importance. Of particular interest is the wedge's flow field and associated thermal structure, which govern: (i) the buoyancy and rheology that control the large-scale dynamics of the mantle wedge and subducting plate; (ii) the breakdown of hydrous minerals and generation of melt; and (iii) the transport of chemical heterogeneity including volatiles into and out of the mantle. Numerical models provide the key to an improved understanding of these processes.

[3] Dynamic models of mantle wedge flow, driven solely by a kinematically prescribed subducting plate, are becoming increasingly realistic, incorporating plausible physical properties (e.g., a stress and temperature-dependent rheology) and matching regional subduction characteristics [e.g., *Syracuse et al*., 2010]. Under such a framework, a corner-flow regime is generated, where viscous drag from the downgoing plate pulls hot mantle material from below the overriding plate into the mantle wedge corner and, subsequently, downward parallel to the subducting slab [e.g., *Davies and Stevenson*, 1992; *Peacock*, 1996; *Peacock and Wang*, 1999; *van Keken et al*., 2002; *Kelemen et al*., 2003]. Conductive thickening of the overriding plate facilitates strong focusing of flow into the mantle wedge corner, which leads to erosion (or "pinching") of the overriding plate and elevated heat flow beneath the fore-arc region [*van Keken et al*., 2002; *van Keken*, 2003]. This, however, is inconsistent with local observations of low heat flow and low seismic attenuation (high Q) [e.g., *Honda*, 1985; *Furukawa and Uyeda*, 1989; *Kincaid and Sacks*, 1997; *Currie and Hyndman*, 2006]. To circumvent this effect, recent models regulate the viscous coupling between downgoing plate and mantle wedge, with reduced coupling generally prescribed from the surface to a depth of around 80 km [e.g., *Conder*, 2005; *Wada and Wang*, 2009; *Syracuse et al*., 2010]. Fully dynamic models, where the subducting slab evolves self-consistently, are likely required for this coupling to evolve naturally [e.g., *Gerya and Yuen*, 2003; *Arcay et al*., 2007].

[4] With such a treatment of plate coupling, plate-driven mantle-wedge models match a wide range of subduction zone observations that are sensitive to wedge temperatures, such as seismic anisotropy [*Kneller et al*., 2007; *Long and Becker*, 2010] and surface topography [*Hebert and Gurnis*, 2010]. They also agree with geochemical constraints on the thermal structure of the downgoing plate [*Plank et al*., 2009], the distribution of intermediate-depth Benioff seismicity [*Abers et al*., 2006] and a correlation of slab parameters, such as subduction velocity and dip angle, with the location of the volcanic arc [e.g., *England et al*., 2004; *England and Wilkins*, 2004; *Syracuse et al*., 2010; *Grove et al*., 2012]. As a consequence, such models are now used in deriving volatile budgets for global subduction [e.g., *Hacker and Abers*, 2004; *van Keken et al*., 2011].

[5] However, other observations, in particular those of a thin lithosphere and high heat flow beneath many back-arc regions [e.g., *Andrews and Sleep*, 1974; *Currie and Hyndman*, 2006], indicate that wedge flow may be more complex than is

implied by these previous studies. The flow field of previous plate-driven models is usually realized by prescribing relatively high viscosities (consistent with a dry mantle) and neglecting the effects of buoyancy (only kinematic effects of subducting plate buoyancy are applied), whilst they are often aided by the choice of boundary conditions. However, at least part of the wedge is likely damp [as is background mantle sampled below mid-ocean ridges, *Hirth and Kohlstedt*, 1996], or wet (due to the introduction of fluids released from the downgoing plate). The production of hydrous melt will extract water from the wedge, thus drying it out where melt is formed [e.g., *Hebert et al*., 2009]. However, the efficiency of dehydration by melt extraction is unclear, as seismic imaging of back-arc mantle reveals extensive low-velocity and high-attenuation anomalies which are easiest explained with high water concentrations [e.g., *Currie and Hyndman*, 2006; *Wiens et al*., 2008; *Hwang et al*., 2011]. If the upper-mantle rheology is damp or wet, upper-mantle viscosities are likely to be low [e.g., *Karato and Wu*, 1993; *Hirth and Kohlstedt*, 1996] and, accordingly, buoyancy will become important in controlling wedge dynamics [e.g., *Davies and Stevenson*, 1992]. Indeed, regional studies indicate that wedge viscosities may be an order of magnitude lower than background mantle [*Billen and Gurnis*, 2001; *Jadamec and Billen*, 2010].

[6] Models that have previously considered these effects produce small-scale convection (SSC), driven by Rayleigh-Taylor instabilities from the base of the overriding plate [e.g., *Honda and Saito*, 2003; *Arcay et al*., 2005; *Currie et al*., 2008; *Wirth and Korenaga*, 2012]. Such instabilities help to explain finger-like seismic velocity patterns below Japan [*Tamura et al*., 2002] and the aforementioned observations of back arcs with thin lithosphere and high heat flow [*Currie et al*., 2008]. They also lead to a transient thermal structure, which has been proposed to explain temporal variations in volcanic activity [*Honda et al*., 2010]. Considered together, these studies [e.g., *Gerya et al*., 2006; *Zhu et al*., 2009, and others] demonstrate that SSC could have a significant effect on wedge thermal structure and, hence, slab dehydration and melt conditions [e.g., *Arcay et al*., 2005, 2006, 2008]. However, thus far, few systematic studies into the factors controlling SSC and its implications for the mantle wedge's flow regime and thermal structure have been undertaken.

[7] Our aims for a set of two papers are: (i) to perform a systematic investigation into the different possible modes of mantle wedge flow, under a range of subduction configurations and rheological parameters; and (ii) to determine their implications for mantle wedge thermal structure. We intentionally keep our setup simple, with subducting plate motion and the coupling between downgoing and overriding plates prescribed kinematically. We also focus on end-member cases of uniform wedge hydration. In this paper, we conduct 2-D analyses, with fully 3-D wedge flow examined in a companion paper. We note that a systematic analysis of SSC in 2-D complements a recent study by *Wirth and Korenaga* [2012], who used a 3-D single-mode approximation to examine SSC within the mantle wedge. Although SSC patterns will vary in 3-D [*Richter*, 1973; *van Hunen et al*., 2003; *Wirth and Korenaga*, 2012], the 2-D models examined herein allow for a wide parameter-space sensitivity study and both a qualitative and quantitative understanding of the dominant controlling mechanisms, which will aid in interpreting any 3-D results. Furthermore, our 3-D models demonstrate that the 2-D simulations are a good representation of the average characteristics of the 3-D system and, as such, the results presented herein provide insights into the magnitude of temperature variations associated with SSC and, accordingly, the likely importance of SSC for slab dehydration and melting.

2. 2-D Model Setup

[8] We follow a standard "kinematic" modeling approach, in which prescribed slab velocities drive fully dynamic flow in the mantle wedge, beneath an overriding plate. We solve the Stokes and energy equations, assuming an incompressible, Bousinessq formulation, using Fluidity, a recently developed finite-element, control-volume code [*Davies et al*., 2011; *Kramer et al*., 2012]. The solution strategy employed for the Stokes equations is identical to that presented in *Davies et al*. [2011], whilst a control-volume method is utilized to solve the energy equation. The accuracy of Fluidity for simulations of this nature has previously been demonstrated via comparisons with a range of analytical and benchmark solutions [*Davies et al*., 2011; *Kramer et al*., 2012]. In addition, Appendix A documents Fluidity's ability to accurately simulate kinematically driven subduction, via comparisons with the well-established benchmark of *van Keken et al*. [2008].

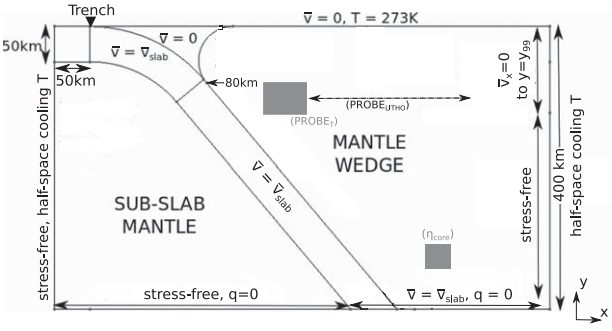

Figure 1. Model setup: the domain is 400 km deep and either 700 or 1110 km wide, for 50° and 30° dip cases, respectively. It is divided into four regions: (i) a prescribed downgoing plate, where $V = V_{slab}$; (ii) a prescribed rigid fore-arc corner, where $V = 0$; (iii) a prognostic mantle wedge; and (iv) a prognostic subslab mantle. Temperature is calculated throughout the computational domain. The subducting slab curves to a constant dip angle at 75 km depth, and is fully coupled to wedge flow below 80 km depth. Temperature boundary conditions follow a half-space cooling relationship everywhere, except at the model's surface (prescribed to 273 K) and base, where a zero heat flux boundary condition, $q = \frac{dT}{dn} = 0$, is enforced. Mechanical boundary conditions are stress-free everywhere except along the top of the overriding plate (fixed), at the base of the wedge (equal to slab velocity, in order to account for the drag which the slab would exert at greater depths) and on the side of the overriding plate, to the depth y_{99}, where temperatures equal 99% of the mantle temperature (in order to compensate for the absence of lithospheric thickening at the boundary). The 50 km^2 gray square (marked η_{core}, centered at 275 km depth and a horizontal distance of 50 km from the slab tip) represents the area where wedge viscosities are analyzed. Temperature transients in Figure 8 are evaluated over the area marked by the 40 × 20 km gray rectangle (labeled PROBE$_T$), centered at 100 km depth, at a horizontal distance of $75 \cdot tan(dip)$km from the wedge corner. The average depth of the 1400 K isotherm, which is used as a proxy for lithospheric thickness in section 3.3, is measured along the horizontal length spanned by the black dotted double-pointed arrow (labeled PROBE$_{LITHO}$), at a horizontal distance of 100–350 km from the wedge corner.

2.1. Geometry, Boundary, and Initial Conditions

[9] Our model setup is illustrated in Figure 1. The subducting plate travels horizontally at the surface for 50 km prior to subduction. It then follows a down-dipping circular arc, to a depth of 75 km, below which it subducts at a constant dip angle. The domain extends to a depth of 400 km, with domain length scaling with slab dip, taking values of 700 and 1110 km, respectively, for 50° and 30° dip cases. Subducting plate velocities are prescribed parallel to the slab surface. A fixed mesh spacing of 1 km is used close to the wedge corner, which increases to 8 km at the domain's base. Such high wedge-corner resolution is necessary to capture the fine-scale dynamics that arises in these complex systems and, additionally, to limit the influence of the well-known pressure "singularity" [e.g., *Davies et al*., 2008; *van Keken et al*., 2008].

[10] Mechanical boundary conditions are stress free on both vertical boundaries (excluding the interface with the incoming plate, where velocities are prescribed to the subduction velocity). By limiting the depth of our domain to 400 km, the deeper slab's influence on the flow regime is not simulated. However, we account for the deeper slab's role by: (i) prescribing a basal wedge outflow boundary condition, equal to the subduction velocity; and (ii) positioning the lower right-hand corner of the domain at a location that approximates the region of influence of the slab, inferred from deeper models. Unlike the majority of previous studies, our overriding plate is not fully fixed or rigid: it is free to evolve self-consistently in response to the local thermal structure and flow field [e.g., *Kelemen et al*., 2003], aside from: (i) at its surface, where we impose a no-slip boundary condition; and (ii) in a curved triangle-shaped region above the subducting plate, where velocities are fixed to zero to a depth of 80 km, thereby yielding the so-called "cold nose," which is consistent with observational constraints [e.g., *Kincaid and Sacks*, 1997; *Rychert et al*., 2008]. Below this depth, however, the subducting slab and mantle wedge are fully coupled, in a manner consistent with the *D80* model of *Syracuse et al*. [2010]. In selected models, where we examine the influence of a step in lithospheric thickness on the underlying flow field (caused, e.g., by a strong craton), the length of the "free" overriding plate is reduced by 200 km and replaced by a 200 km thick square, with a viscosity of 10^{24} Pa s, in the upper right-hand corner of the domain.

[11] The surface temperature, T_s, is fixed to 273 K, whilst side temperature boundary conditions follow an error function:

$$T(x=0,y) = T_s + (T_0 - T_s)\mathrm{erf}\left(\frac{y}{2\sqrt{\kappa t_{plate}}}\right). \quad (1)$$

[12] Here T_0 is the reference mantle temperature (fixed at 1623 K), t_{plate} is either the subducting slab age, t_{subd}, or the overriding plate age, t_{upper}, and κ is thermal diffusivity. Equation (1) is utilized in defining initial conditions, with $t_{plate} = t_{subd}$ imposed within the subducting plate and t_{plate}

Table 1. Nomenclature and Reference Values for 2-D Model Parameters Used in this Paper

Quantity	Symbol	Reference Value
Gravity	g	9.81 ms^{-2}
Reference density	ρ_0	3300 $kg\,m^{-3}$
Mantle temperature	T	T_0=1623 K=1350°C
Surface temperature	T_s	T_s=273 K=0°C
Thermal conductivity	k	3.1 $Wm^{-1}K^{-1}$
Specific heat capacity (constant pressure)	c_p	1250 $Jkg^{-1}K^{-1}$
Thermal diffusivity	κ	0.75×10^{-6} m^2s^{-1}
Thermal expansivity	α	2.5×10^{-4} K^{-1}
Activation energy—dry diffusion creep	$E_{diff,d}$	375 $kJ\,mol^{-1}$
Activation energy—dry dislocation creep	$E_{disl,d}$	530 $kJ\,mol^{-1}$
Activation energy—hydrated diffusion creep	$E_{diff,h}$	335 $kJ\,mol^{-1}$
Activation energy—hydrated dislocation creep	$E_{disl,h}$	480 $kJ\,mol^{-1}$
Activation volume—dry diffusion creep	$V_{diff,d}$	6×10^{-6} $kJ\,mol^{-1}$
Activation volume—dry dislocation creep	$V_{disl,d}$	20×10^{-6} $kJ\,mol^{-1}$
Activation volume—hydrated diffusion creep	$V_{diff,h}$	4×10^{-5} m^3mol^{-1}
Activation volume—hydrated dislocation creep	$V_{disl,h}$	11×10^{-5} m^3mol^{-1}
Power-law exponent	n	3.5
Maximum viscosity	η_{max}	10^{24} Pa s
Reference grain size	g_0	10 mm
Universal gas constant	R	8.3145 $J\,mol^{-1}K^{-1}$
Water content—damp mantle	$C_{OH,damp}$	1000 H/10^6Si
Water content—wet mantle	$C_{OH,wet}$	3000 H/10^6Si
Water content—very wet mantle	$C_{OH,v.wet}$	5000 H/10^6Si
Water content exponent	r	1.2
Preexponential constant—dry diffusion creep	A_d	$10^{8.82}$ Pa s
Preexponential constant—dry dislocation creep	B_d	$10^{\frac{-11.04}{n}}$ Pa $s^{\frac{1}{n}}$
Preexponential constant—hydrated diffusion creep	$A_{h,0}$	10^{12} Pa $s\frac{H}{10^6Si}^{\frac{r}{n}}$
Preexponential constant—hydrated dislocation creep	$B_{h,0}$	$10^{\left(6+\frac{1.95}{n}\right)}$ Pa $s^{\frac{1}{n}}\cdot\frac{H}{10^6Si}^{\frac{r}{n}}$

$=t_{upper}$ imposed in the mantle wedge, for all cases. We note that the fixed-temperature boundary condition on the right-hand side of the domain does not account for lithospheric conductive cooling and thickening of the overriding plate over time. To minimize this boundary effect, we enforcing a no normal-flow boundary condition down to a depth where temperature reaches a nominal value of 99% of mantle temperature.

[13] Models are initialized until the thermal signature of the downgoing plate is advected to the base of the domain. In our results, we refer to the time when the slab reaches 400 km depth as $t = 0$. After a further ≈ 10 Myr, wedge flow patterns stabilize into a single mode, although they do evolve further as the overriding plate thickens conductively. We analyze our results in the $t = 10$–100 Myr time window. However, for analyzing upper-plate thickening we will refer to cooling time t_{cool} since the model start, as the lithosphere already thickens during the initialization phase of the model.

2.2. Material Properties

[14] Material properties are summarized in Table 1. Standard values are used for equation of state parameters, and these do not vary spatially. For viscosity, a composite diffusion and dislocation creep rheology is utilized. Olivine is assumed to be the dominant constituent of the upper mantle, so that the following laws can be used:

$$\eta_{diff,x}(T)=A_x\exp\left(\frac{E_{diff,x}+(PV_{diff,x})}{RT}\right), \quad (2)$$

$$\eta_{disl,x}(T,\dot{\bar{\epsilon}})=B_x\exp\left(\frac{E_{disl,x}+(PV_{disl,x})}{nRT}\right)\dot{\bar{\epsilon}}^{\frac{(1-n)}{n}}, \quad (3)$$

where the subscript x is d for cases with a dry rheology and h for cases where a hydrated rheology is introduced. Subscripts diff and disl denote diffusion creep and dislocation creep. The exponent n in the power-law relationship between viscosity, η_{disl}, and the second-invariant of the strain rate tensor, $\dot{\bar{\epsilon}}$, accounts for the effects of stress dependence under dislocation creep. T and P represent absolute temperature (for which an adiabatic gradient of 0.5 K/km is added to our Boussinesq potential temperature solution) and lithostatic pressure ($P=\rho_0 gh$, where h is depth), respectively. R is the universal gas constant. The activation energies (E_{diff} and E_{disl}) and volumes (V_{diff} and

V_{disl}) are taken from *Hirth and Kohlstedt* [2003]. Together with the other parameter values, these are listed in Table 1. The prefactors for dry rheology, A_d and B_d, are constants, while those for hydrated rheologies include a water content term:

$$A_h = A_{h,0}\, C_{OH}\,, \tag{4}$$

$$B_h = B_{h,0}\, (C_{OH}^{-r})^{\frac{1}{n}}. \tag{5}$$

[15] Here C_{OH} and r represent the water content and water content exponent, respectively [*Hirth and Kohlstedt*, 2003]. We do not include a stress-limiting rheology, but, instead, truncate viscosity at a fixed maximum η_{max} of 10^{24} Pa, yielding effective diffusion and dislocation viscosities $\eta_{diff,eff.}$ and $\eta_{disl,eff.}$ as follows:

$$\eta_{diff,eff.} = \left(\frac{1}{\eta_{diff}} + \frac{1}{\eta_{max}}\right)^{-1}, \tag{6a}$$

$$\eta_{disl,eff.} = \left(\frac{1}{\eta_{disl}} + \frac{1}{\eta_{max}}\right)^{-1}. \tag{6b}$$

[16] Diffusion and dislocation creep laws are, in turn, combined via a harmonic mean, to obtain a composite creep viscosity:

$$\eta_{comp} = \left(\frac{1}{\eta_{diff,eff.}} + \frac{1}{\eta_{disl,eff.}}\right)^{-1}. \tag{7}$$

2.3. Model Cases

[17] To unravel the dominant controls on the mantle wedge's flow regime and thermal structure, we examine a suite of simulations, where we systematically vary a range of subduction parameters. To examine the role of viscosity, we vary wedge hydration between dry, "damp" [$C_{OH} = 1000\,H/10^6 Si$—representative of subridge mantle, *Hirth and Kohlstedt*, 1996], wet ($C_{OH} = 3000 H/10^6 Si$) and very wet ($C_{OH} = 5000\,H/10^6 Si$)—as end-member subduction-zone hydration cases [e.g., *Karato*, 2003; *Katz et al.*, 2003]. Hydration is assumed to be constant throughout the wedge. We also vary the subduction velocity, over a representative range: 2 cm/yr—slow; 5 cm/yr—intermediate; and 10 cm/yr—fast [e.g., *Lallemand et al.*, 2005; *Syracuse and Abers*, 2006; *Seton et al.*, 2012]. For the overriding plate, we consider relatively young (50 Myr) and old (120 Myr) cases. The age of the downgoing plate is always set to 50 Myr at the trench, as we found that subducting slab age has a negligible effect on wedge temperatures and flow, consistent with results from *Wirth and Korenaga* [2012]. We refer to the aforementioned set of models as our reference models.

[18] The remainder of this article is structured as follows: in section 3, we illustrate the different flow regimes that arise as a consequence of the aforementioned variations, and discuss the key controlling parameters. In section 4, we examine cases with several variations that are not listed above, highlighting additional complexities that do not become apparent in our reference models: (i) models with a slab dip of 30°; (ii) models where we impose a strong lithospheric block in the top right-hand corner of the domain; and (iii) models where we include excess hydration in the wedge corner only. In section 5, we discuss the impacts of the different flow regimes on wedge thermal structure, with conclusions and avenues for future work discussed in section 6

3. Flow Styles, Characteristics, and Primary Controls

[19] In this section, results are described in terms of wedge flow styles and characteristics, using the set of reference models described in section 2.3. The parameters exerting the main control on the flow regime are also highlighted.

3.1. Flow Regimes

[20] We observe two distinct flow regimes in the mantle wedge, across the parameter space examined (Figure 2):

[21] 1. Corner flow: this flow regime exhibits a stable velocity pattern. Strong coupling between the downgoing slab and the mantle wedge drags sublithospheric material toward the wedge corner, where it induces local erosion, or "pinching" of the overriding plate [e.g., *van Keken et al.*, 2008], and then downward parallel to the slab (Figure 2a). Such a stable flow configuration allows for relatively unperturbed conductive cooling and thickening of the overriding plate. In previous wedge flow studies, this mode has been promoted by: (i) focusing on flow dynamics under a dry rheology, with wedge-core viscosities that are at, or above, the upper-mantle average of 10^{21} Pa s; (ii) neglecting buoyancy effects; or (iii) prescribing boundary conditions from corner-flow solutions [e.g., *van Keken et al.*, 2002; *Hasenclever et al.*, 2011].

[22] 2. Small-scale convective (SSC) flow: in this unsteady flow regime instabilities develop at the base of the overriding plate. In such cases, a

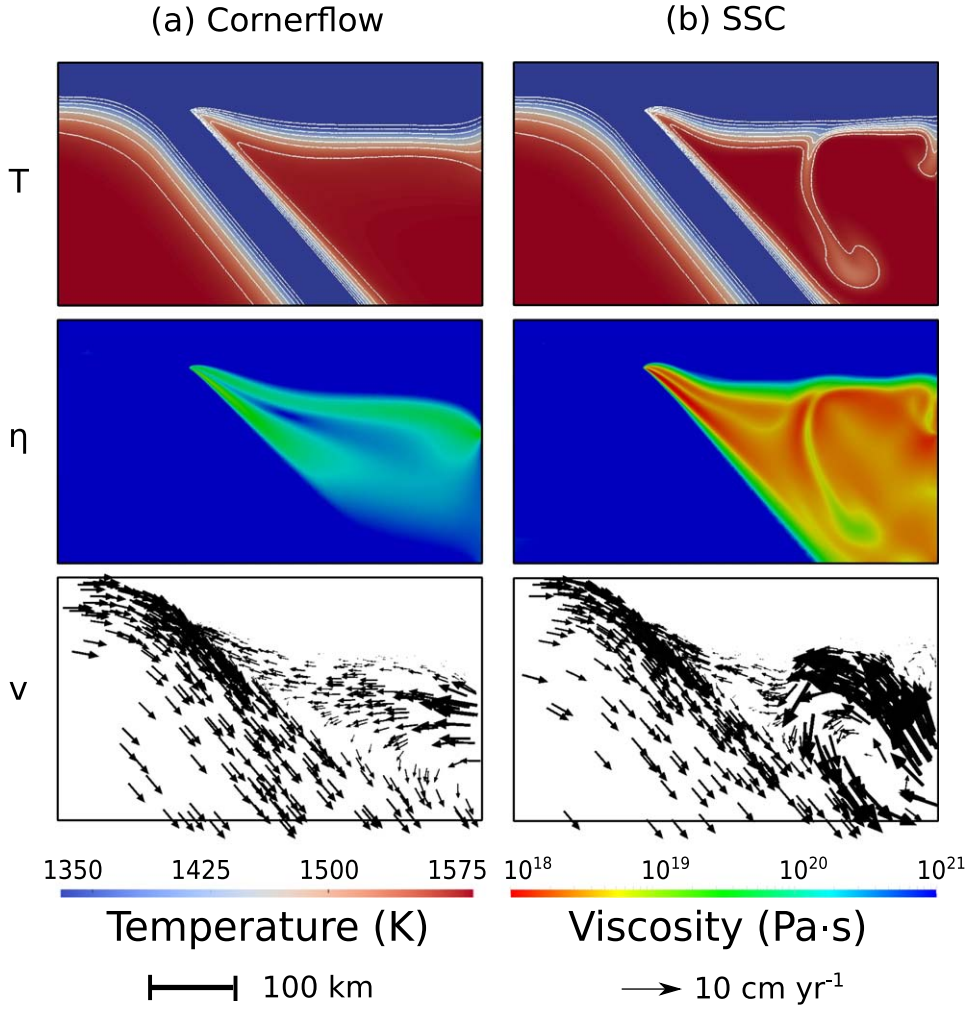

Figure 2. Thermal structure (T), viscosity (η), and corresponding velocity vectors (V) for a selection of our reference cases with: (a) corner flow; and (b) small-scale convection (SSC). The models illustrated have a 120 Myr old upper plate, intermediate subduction velocities of 5 cm/yr, with (a) dry and (b) wet (C_{OH} =3000 $H/10^6Si$) rheologies, respectively. Temperature contours range from 1320 to 1620 K, in 50 K intervals.

corner-flow type of drag persists to some degree, so that after formation, instabilities are advected toward the wedge corner. Once developed, instabilities can attain velocities that exceed the subduction velocity (Figure 2b). Previous studies have found that SSC is promoted by low mantle viscosities, as is expected from wedge hydration [e.g., *Honda and Saito*, 2003; *Arcay et al.*, 2005; *Currie et al.*, 2008; *Wirth and Korenaga*, 2012].

[23] In corner-flow models, wedge viscosity is largely dominated by diffusion creep. However, dislocation creep leads to the formation of two low-viscosity areas in regions of high strain rate: (i) close to the wedge corner, above the interface with the downgoing plate; and (ii) below the upper plate (Figure 2a). The former, identified in the literature as a "subduction channel" [e.g., *Hebert et al.*, 2009], stretches from the minimum depth of plate decoupling, down to 150–250 km depth; its thickness ranges between 5 and 25 km. As would be expected, in cases with SSC, wedge viscosities are generally reduced, whilst local contrasts are observed, arising due to spatial variations in temperature and strain rates: where instabilities propagate from the lithosphere's base into the wedge core, regions of higher viscosity can be observed (lower temperatures), which are surrounded by low-viscosity zones (higher strain rates), thus easing their passage through the mantle wedge (Figure 2b).

[24] The flow regime's characteristics are best illustrated via horizontal velocity profiles, normalized

against slab velocity. Velocities change through time, as flow patterns evolve and/or the lithosphere thickens through diffusive cooling. Examples of superimposed snapshots, at intervals of 0.5 Myr, for model times of 10–40 Myr, on a horizontal line at a constant depth of 200 km (i.e., below the overriding plate), are presented in Figure 3. At this depth, corner-flow cases (top row) exhibit smooth horizontal velocity profiles, since the flow pattern is regular and approximately steady state. In SSC-dominated models (middle and bottom rows), sublithospheric instabilities manifest themselves as transient fluctuations in the horizontal velocity profiles. Note that the passage of individual instabilities across the wedge can be registered by more than one snapshot. As cases become more unstable, mantle wedge velocities can exceed those of the subducting slab.

[25] In a few cases (e.g., Figure 3i), a decoupled convective "cell" develops at some distance from the slab. In such cases, a positive horizontal velocity near the right-hand boundary, associated with a flip in the direction of flow, identifies a decoupled "cell." This decoupled "cell" is only apparent in some cases, promoted by a combination of low wedge viscosity and low plate velocity. This flow cell is amplified in our models by the fixed temperature, stress-free boundary condition imposed at the right-hand sidewall. Nonetheless, these cases show that, under certain conditions, the slab can be inefficient at driving wedge flow.

3.2. Styles of Small-Scale Convection

[26] Two end-member styles of SSC are observed across the parameter space examined, with Table 2 summarizing our classification for all cases. In the most unstable "SSC-drip" models (Figure 4a), SSC takes the form of cold, Rayleigh-Taylor type instabilities, which are nucleated in the back-arc region. Here cold sublithospheric material begins to detach, forming downwelling plume-like structures, which penetrate into the wedge core. These cold drips are more viscous than the surrounding mantle wedge. Due to the non-Newtonian rheology, these drips are surrounded by low-viscosity zones, which ease their passage through the mantle wedge. They grow more rapidly than they are swept away by background wedge flow, but are, nonetheless, advected toward the wedge corner, where they induce thermal fluctuations of 50–100 K (variations in the thermal structure are discussed, in detail, in section 5).

[27] "SSC-ripple" cases (Figure 4b) exhibit instabilities in the form of cold ripples, which remain rooted to the lithosphere's base and rapidly migrate toward the wedge corner after forming, as a consequence of background corner flow. In comparison to SSC-drip cases, these ripples have less of an influence on the thermal structure of the wedge core (e.g., their expression is more difficult to observe in Figure 4b). However, they display a comparable influence in the wedge corner, temporarily reducing local temperatures by 50–100 K. As will be discussed further in section 3.4, instabilities of this form are most notably observed below overriding plates that experience high sublithospheric shearing (i.e., cases with high subduction velocities), which does not allow sufficient time for instabilities to develop into drips.

3.3. Evolution of Upper-Plate Lithospheric Thickness

[28] Small-scale convection is a consequence of upper-plate instability and, accordingly, upper-plate thickness evolves differently under corner-flow and SSC regimes. It is therefore insightful to examine its evolution over time. We track the 1400 K isotherm as a proxy of thermal lithospheric thickness, averaging over a horizontal distance that approximately spans the back-arc length (see the double-pointed dash-dotted arrow, labeled PROBE_{LITHO}, in Figure 1), with results presented in Figure 5. Note that by model $t = 0$, the upper plate has cooled for $t_{\mathrm{cool}} = 5$, 10, and 25 Myr, respectively, for fast (10 cm/yr), intermediate (5 cm/yr), and slow (2 cm/yr) cases and, hence, upper plates differ in thickness, at $t = 0$. We display for each case, lithospheric thickness evolution up to a total upper-plate cooling age of $t_{\mathrm{cool}} = 105$ Myr (i.e., until a model time $t = 100$, 95, and 80 Myr, for fast, intermediate, and slow cases, respectively). This allows for a comparison of final thicknesses.

[29] For corner-flow cases with a dry wedge rheology, an unperturbed conductive thickening of the upper plate is observed. Cases that exhibit SSC also display an average thickening trend with age. However, for the most unstable cases (i.e., those with the highest water content) we observe transient fluctuations in lithospheric thickness, with: (i) intervals of lithospheric thickening at higher rates than the conductive dry case, which correspond to periods where lithospheric instabilities are growing; and (ii) sudden decreases in lithospheric thickness, when instabilities detach from the upper plate. The net effect is that the lithosphere thickens less in SSC cases, when compared

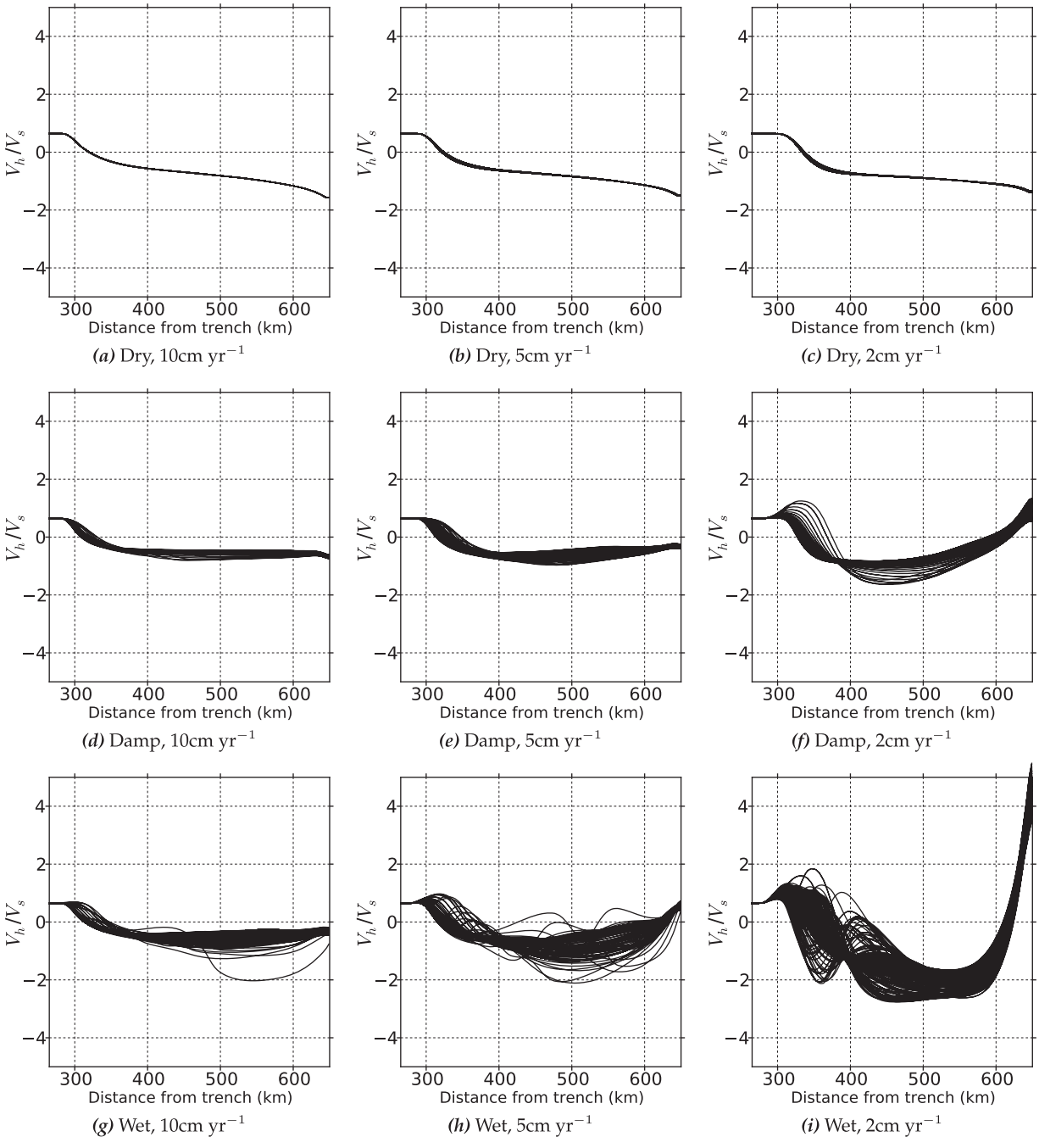

Figure 3. Horizontal velocities at 200 km depth, normalized to slab velocity for: (a–c) dry; (d–f) damp ($C_{OH}=1000\,H/10^6Si$); and (g–i) wet ($C_{OH}=3000\,H/10^6Si$) models with 120 Myr old upper plates. Superimposed horizontal velocity snapshots are shown, at 0.5 Myr intervals, for a simulation time of 10–40 Myr. Smooth and irregular profiles, respectively, pertain to corner flow and SSC modes; a few of the slowest cases form a decoupled "cell" with a positive horizontal velocity close to the right-hand boundary. Positive velocities, on the left of each plot, are associated with return wedge flow immediately above the slab surface.

to dry corner-flow cases. We note that some of the damp cases examined are an exception to this rule, with thickening more rapid than the dry cases over comparable time-intervals. Analysis of the underlying dynamics demonstrates that in such cases an instability is in the process of forming beneath the lithosphere. However, the timescale for such instabilities exceeds our simulation time (and likely

Table 2. Summary of Model Cases[a]

Dip (°)	V_{slab} (cm yr^{-1})	T_{upper} (Myr)	C_{OH} (H/10^{6}Si)	η_{wedge} (Pa s)	$\eta_{channel}$ (Pa s)	Flow Regime
30	5	50	0	2.7×10^{20}	3.4×10^{19}	Corner flow
30	5	50	1000	1.1×10^{19}	3.4×10^{18}	Corner flow
30	5	50	3000	4.5×10^{18}	2.2×10^{18}	SSC-drips
30	5	50	5000	2.9×10^{18}	1.8×10^{18}	SSC-drips
50	2	50	0	4.6×10^{20}	1.0×10^{20}	Corner flow
50	2	50	1000	1.2×10^{19}	7.1×10^{18}	Corner flow
50	2	50	3000	5.4×10^{18}	4.1×10^{18}	SSC-drips (decoupled cell)
50	2	50	5000	3.4×10^{18}	2.5×10^{18}	SSC-drips (decoupled cell)
50	5	50	0	2.9×10^{20}	3.3×10^{19}	Corner flow
50	5	50	1000	1.0×10^{19}	3.3×10^{18}	Corner flow
50	5	50	3000	3.7×10^{18}	1.6×10^{18}	SSC-drips
50	5	50	5000	2.7×10^{18}	1.2×10^{18}	SSC-drips (decoupled cell)
50	10	50	0	1.9×10^{20}	1.7×10^{19}	Corner flow
50	10	50	1000	7.9×10^{18}	2.4×10^{18}	Corner flow
50	10	50	3000	3.4×10^{18}	1.1×10^{18}	SSC-drips
50	10	50	5000	2.1×10^{18}	7.7×10^{17}	SSC-drips (decoupled cell)
50	2	120	0	4.0×10^{20}	1.3×10^{20}	Corner flow
50	2	120	1000	1.2×10^{19}	8.2×10^{18}	SSC-ripples
50	2	120	3000	4.9×10^{18}	3.9×10^{18}	SSC-drips
50	2	120	5000	3.0×10^{18}	2.5×10^{18}	SSC-drips (decoupled cell)
50	5	120	0	2.4×10^{20}	4.2×10^{19}	Corner flow
50	5	120	1000	1.0×10^{19}	3.9×10^{18}	SSC-ripples
50	5	120	3000	3.9×10^{18}	1.9×10^{18}	SSC-drips
50	5	120	5000	2.4×10^{18}	1.2×10^{18}	SSC-drips (decoupled cell)
50	10	120	0	1.6×10^{20}	2.1×10^{19}	Corner flow
50	10	120	1000	7.8×10^{18}	2.4×10^{18}	SSC-ripples
50	10	120	3000	3.4×10^{18}	1.2×10^{18}	SSC-ripples
50	10	120	5000	2.1×10^{18}	8.7×10^{17}	SSC-drips

[a]For each, slab dip, slab velocity V_{slab}, upper-plate age T_{upper}, wedge water content C_{OH}, wedge-core viscosity η_{wedge}, subduction channel viscosity $\eta_{channel}$ and the flow regime are given.

also those available in natural subduction zones, before other changes in the system occur) and, consequently, these instabilities are unable to develop fully.

3.4. Principal Flow Style Controls—Subduction Velocity, Wedge Viscosity, and Upper-Plate Age

[30] Figure 6 documents how variations in subduction velocity and wedge hydration relate to the different flow regimes for cases with young (50 Myr) and old (120 Myr) upper plates. Grayscale indicates the extent to which the downgoing plate is able to drive corner flow with black rectangles for pure corner flow, and lighter gray ellipses for cases with a mix of SSC and corner flow, decreasing in shade as the coupling becomes less efficient. SSC ellipses stand up for drips and lie flat for ripples. Ellipses with an additional dot indicate that instabilities mainly nucleate at model edges. Average wedge-core viscosity is annotated, measured within a 25 km square box, located 50 km to the right of the slab tip at 350 km depth—marked η_{core}, in Figure 1 (i.e., at a location where mantle mixing is high and velocity fluctuations are minimal).

[31] We find that cases with a 200 Myr old upper plate are somewhat more unstable than those with a 50 Myr old upper plate (cf. e.g., damp cases in Figure 6, which exhibit an unstable SSC regime for the former, but a stable corner-flow regime for the latter). Sublithospheric instabilities arise due to the lithosphere's negative buoyancy, which increases with upper-plate age and, hence, this trend is easy to understand.

[32] Instability formation is resisted by viscous forces (and thermal diffusion), and thus the propensity for SSC increase with the local Rayleigh number [*Davaille and Jaupart*, 1994]. As such, we observe that dry cases, with higher wedge viscosities, exhibit a corner-flow pattern, whereas SSC becomes more common with increasing wedge hydration and, hence, decreasing wedge viscosities. As with previous studies, we find that wedge viscosities below a threshold value of $\approx 5 \times 10^{18}$ Pa s are necessary for the development of Rayleigh-Taylor instabilities at the base of the lithosphere [e.g., *Honda and Saito*, 2003; *Wirth and Korenaga*, 2012].

[33] Whilst the occurrence of SSC is principally dictated by wedge viscosity and upper-plate age, subduction velocity controls the style. Higher

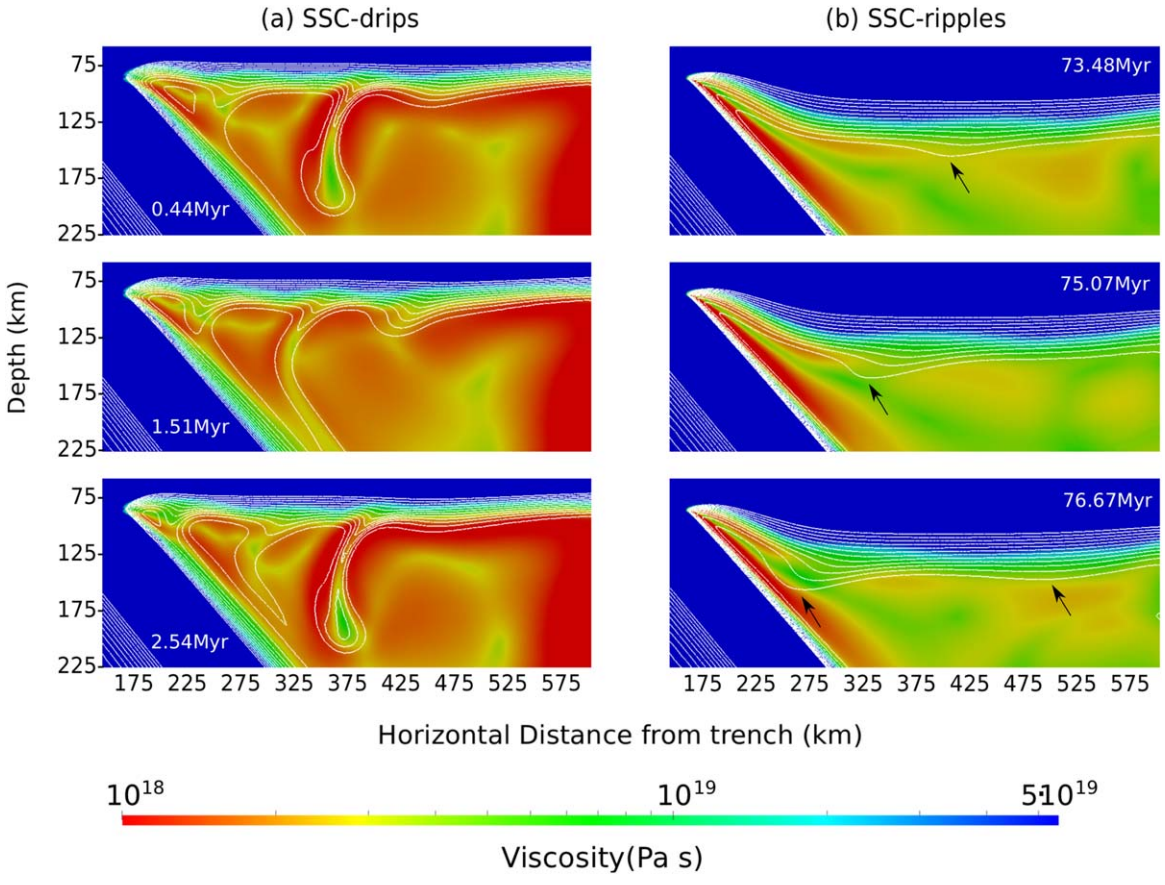

Figure 4. Different styles of small-scale convection (SSC): (a) "drips," which are nucleated in the back-arc region and subsequently penetrate into the wedge core; and (b) "ripples," which remain rooted to the lithosphere's base and rapidly migrate toward the wedge corner after forming. Ripples can be identified by tracking the transient sublithospheric bulge in the warmest temperature contour plotted (highlighted by dark arrows). These snapshots are from cases with (a) a very wet (C_{OH} =5000H/10^6Si), 2 cm/yr subduction velocity, 50 Myr old upper-plate case; and (b) a wet (C_{OH} =3000H/10^6Si), 10cm/yr subduction velocity, 120 Myr old upper-plate case. Temperature contours range from 1320 to 1620 K, in 25 K intervals, revealing comparable temperature fluctuations between fully developed drips and sheared ripples, upon interaction with the wedge corner. In all SSC cases, asthenospheric viscosities are below 10^{19} Pa s.

subduction velocities lead to a stronger corner flow, which: (i) thins the lithosphere and, hence, the thickness of the layer available for destabilization (see Figure 5—in dry and damp corner-flow cases the lithosphere thickens conductively, but is affected by flow shearing. As a result back-arc lithosphere is about 10 km thinner for a case with a subduction velocity of 10 cm/yr, when compared to a case with a subduction velocity of 2 cm/yr. In wet and very wet cases, where SSC develops, subduction velocity has less of an effect on lithospheric thickness); and (ii) shears instabilities before they can fully develop. As such, the style of SSC changes with increasing subduction velocity. For example, for a wet wedge below a 120 Myr old upper plate, the instabilities at a subduction velocity of 10 cm/yr take the form of ripples rather than the drips observed at subduction velocities of 2 and 5 cm/yr.

[34] The attenuating effect of shearing velocity on the development of (2-D) SSC that we find is consistent with a range of other analytical and numerical studies [*Richter*, 1973; *van Hunen et al*., 2003; *Huang et al*., 2003], which assume a stress-independent rheology. However, it is opposite to the findings of *Currie et al*. [2008], who attribute their result to a strong strain rate softening, where higher subduction velocities lead to a stronger corner flow, which reduces effective viscosities in the mantle wedge. Their strong softening is likely due to the inclusion of a highly strain rate dependent

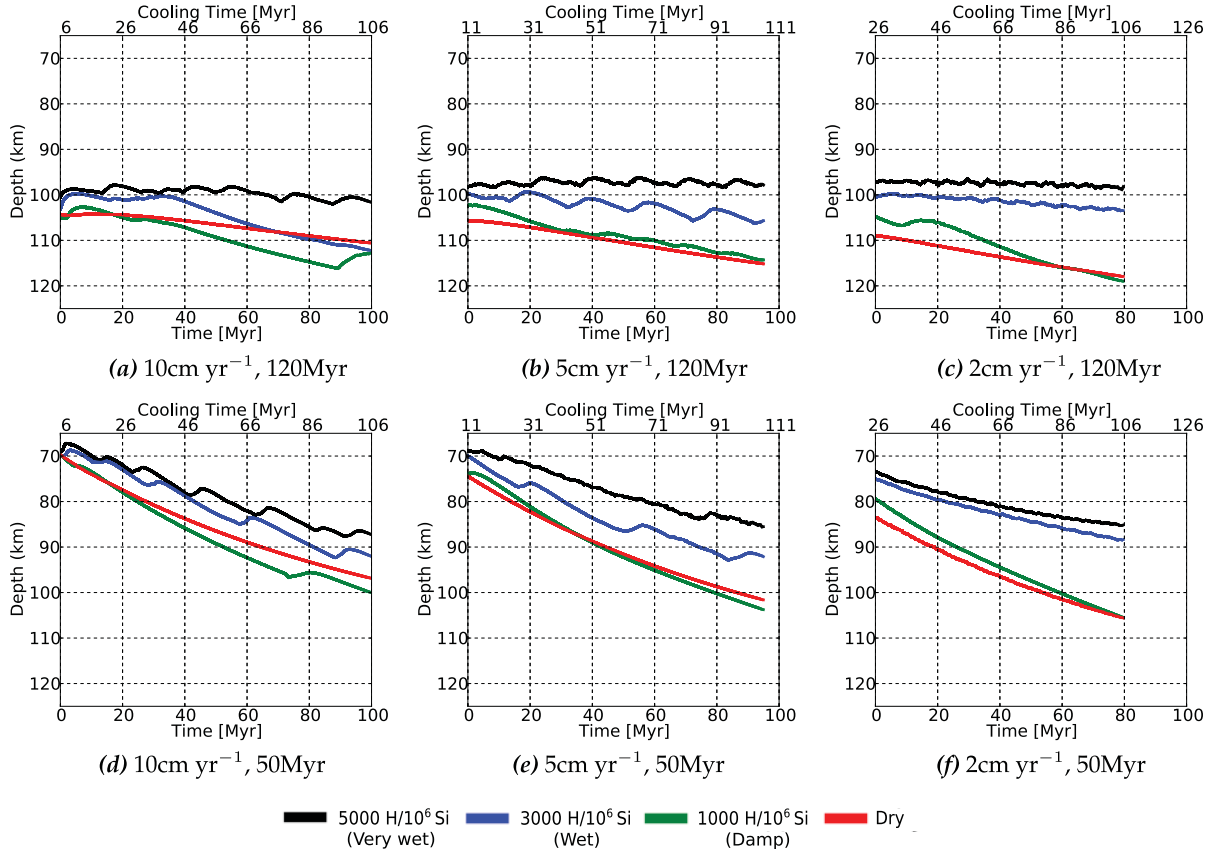

Figure 5. Temporal evolution of the 1400 K isotherm's depth (which we use as a proxy for lithospheric thickness), horizontally averaged between 100 km and 350 km from the wedge corner (labeled $\text{PROBE}_{\text{LITHO}}$ in Figure 1), for all 50°-dip cases. The figures illustrate the sensitivity of lithospheric thickness to subduction velocity, (hydration-dependent) viscosity and overriding plate age. In dry corner-flow cases, the overriding plate monotonically thickens with time through diffusive cooling. For wet and very wet cases, small-scale convection can lead to transient and local periods of thinning, which are associated with detaching drips, thereby counteracting the process of conductive thickening. Cases with an older (120 Myr old) upper plate are generally more unstable than those with a younger (50 Myr old) upper plate.

plastic deformation mechanism. By contrast, in our models, strain softening is insufficient to outweigh other intrinsic viscosity factors and, accordingly, we observe that the growth of instabilities is stunted at high subduction velocities.

3.5. SSC Timescales

[35] To further understand what governs SSC, we have analyzed instability timescales (i.e., the time interval between individual instabilities). Figure 7 illustrates the temporal evolution of temperature, in a box at the base of the plate, near the wedge corner (labeled PROBE_T in Figure 1). The box was chosen to best capture the instabilities that form: instabilities are spawned from different locations at the base of the overriding plate, but all are advected toward the mantle wedge corner (i.e., close to this corner, most are detected—only a few instabilities die out before reaching the detection box). For dry cases, we observe a steady flow regime, with no drips. Conversely, in very wet, wet and, occasionally, damp cases, drips manifest themselves as sharp reductions in temperature, as they traverse our detection box.

[36] Across the parameter space examined, the time interval between instabilities generally (note—there are exceptions) increases: (i) with increasing wedge viscosity (cf. e.g., wet and very wet cases in Figures 7b and 7c); (ii) with increasing subduction velocity (cf. e.g., very wet cases in Figures 7d–7f); (iii) for thicker (older) upper-plate lithosphere (cf. e.g., wet and very wet cases in

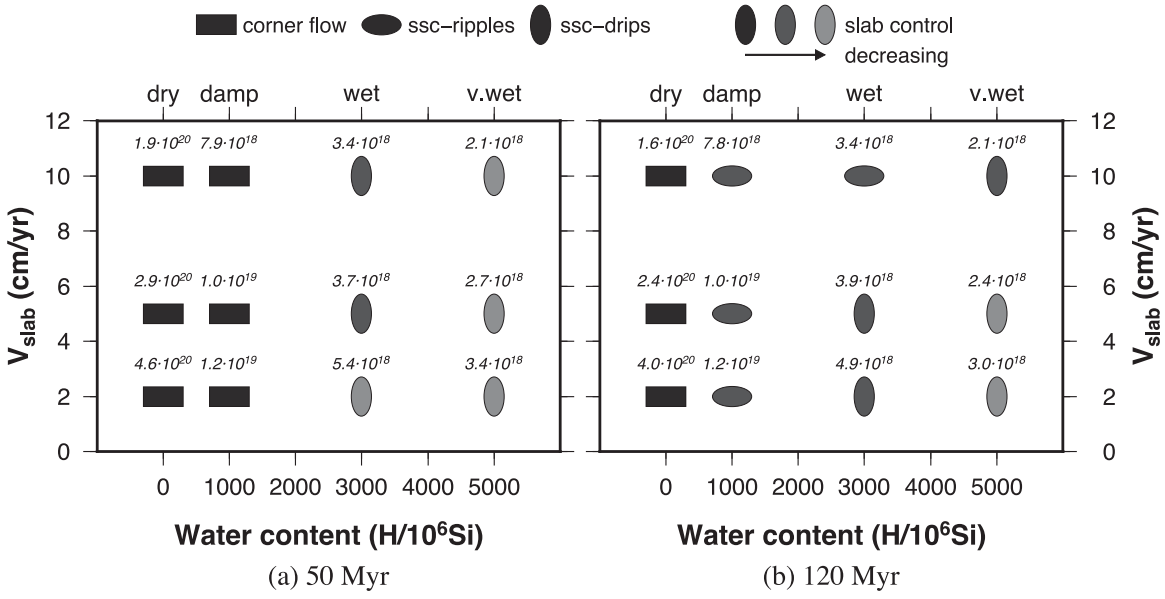

Figure 6. Wedge flow style as a function of slab velocity and wedge hydration, for cases with: (a) 50 Myr old; and (b) 120 Myr old overriding plates, respectively. Symbols denote the observed flow regime: rectangles, horizontal ellipses, and vertical ellipses indicate corner flow, SSC ripples and SSC drips, respectively. Light to dark grayscale shading represents the degree of coupling between slab and wedge. Annotations indicate wedge-core viscosities (η_{core} of Figure 1), in Pa s.

Figures 7c–7f). The first two trends are as expected from the previous section. The third trend is, at first, surprising, as we have found older lithosphere to be more unstable than younger lithosphere, yet instability timescales are longer. Although one might intuitively expect thickness of the unstable layer to be proportional to lithospheric thickness, we find that the unstable layer thickness (either estimated from temperature-depth profiles or from the difference in lithospheric thickness between corner-flow and SSC cases) is similar for old and young upper plates. In fact, scaling analyses by *Davaille and Jaupart* [1994] predict that unstable layer thickness depends on mantle temperature and activation energy of viscosity only (i.e., not on plate age). We attribute the different timescales for drips of old and young plates to the depth dependence of viscosity which leads to higher viscosities in the old-plate unstable layer and, hence, lower local Rayleigh numbers and longer timescales.

[37] There are additional complexities in this unstable dynamic system, which may explain why instability timescales in some models differ to the trends described above. Instabilities in SSC ripple cases exhibit different timescales to those of SSC drip cases. Furthermore, drip amplitudes can vary for individual cases (Figure 7), sometimes alternating between strong and weak drips, which are the result of different or interacting instabilities. Instabilities often spawn at different locations and, in some cases, multiple instabilities can coexist. In the most unstable cases, drips tend to form in the back arc were the upper-plate thickness is relatively constant. In other instances, the region where the lithosphere starts to pinch above the wedge corner serves to localize an additional, or the only, instability. Instabilities that form closer to the wedge corner have less time to grow and, therefore, have a different amplitude to those forming adjacent to model's right-hand side. Multiple drips can also coalesce near the wedge corner, resulting in variable amplitudes. The net result is that although timescales exhibit some general trends with wedge parameters, these do not always hold.

4. Additional Controls: Upper-Plate Length

[38] As demonstrated in sections 3.4 and 3.5, the thermal structure and flow regime of the mantle wedge are principally controlled by rheological variations, upper-plate age and subduction velocity. Slab age has little influence on wedge

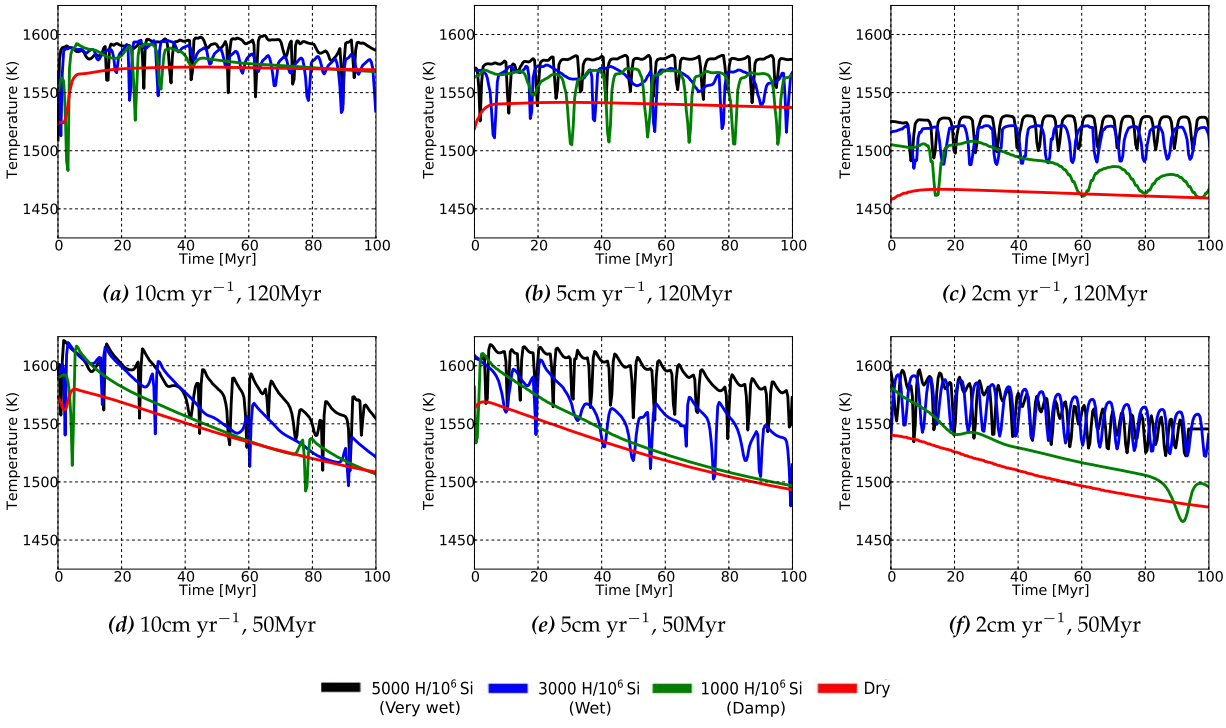

Figure 7. Thermal evolution of the sublithospheric area, labeled "PROBE$_T$" in Figure 1, for: (a–c) old; and (d–f) young overriding plates, as a function of wedge hydration and subduction velocity. Drips propagating through the box result in transient low-temperature troughs. Older, thickened plates destabilize more efficiently, promoting small-scale convection in all hydrated cases. Increased hydration leads to more unstable behavior, which is characterized by smaller and more regular time intervals between drips.

dynamics, however, some other parameters, such as slab dip, local variations in upper-plate thickness, and variable wedge hydration are significant, as it turns out, mainly because they control the length of the upper plate that is available for destabilization. In this section, we examine the modifying role of these factors.

4.1. Slab Dip

[39] To investigate how slab dip influences SSC, we discuss the results from additional cases where the subducting plate dips at angle of 30° (these cases have an intermediate subduction velocity of 5 cm/yr and a 50 Myr old upper plate). We found that cases with a higher slab dip angle of 70° were mostly inefficient at driving wedge-corner flow and, hence, could not be compared. Figures 8a–8c illustrate the temporal evolution of temperature, in the box labeled PROBE$_T$ in Figure 1, for the 30° cases. We observe SSC for 30° and 50° dip models, under approximately the same conditions (i.e., under a wet and very wet rheology). However, for cases with a wet rheology, the time interval between instabilities decreases for the 30° dip cases, whilst instabilities are also more regularly spaced, in comparison to the 50° dip case. Such differences are principally controlled by the longer upper plate in the 30° cases: as can be seen for the dry, conductively thickening cases (Figures 8a and 8b), the larger domain (x dimension of 1100 km) of the 30° dip cases allows for more conductive thickening in comparison to the 50° dip cases (x dimension of 700 km), thus increasing the thickness of the unstable layer. In addition, the increased upper-plate length of the 30° cases provides additional space for instabilities to form according to their intrinsic wavelength (rather than being controlled by model boundaries), thus explaining the more regular destabilization pattern. The intrinsic wavelength of instabilities in the very wet cases is smaller than the upper-plate length for the 50° dip cases (around 150 km) and, hence, for these cases, the effect of dip (and upper-plate length) is less pronounced. However, we note that lithospheric thinning for both wet and very wet cases is more efficient in the smaller dip models (Figures 8d and 8e).

[40] These results illustrate the complex nature of this system. While we could design a set of models where upper-plate length does not vary with dip,

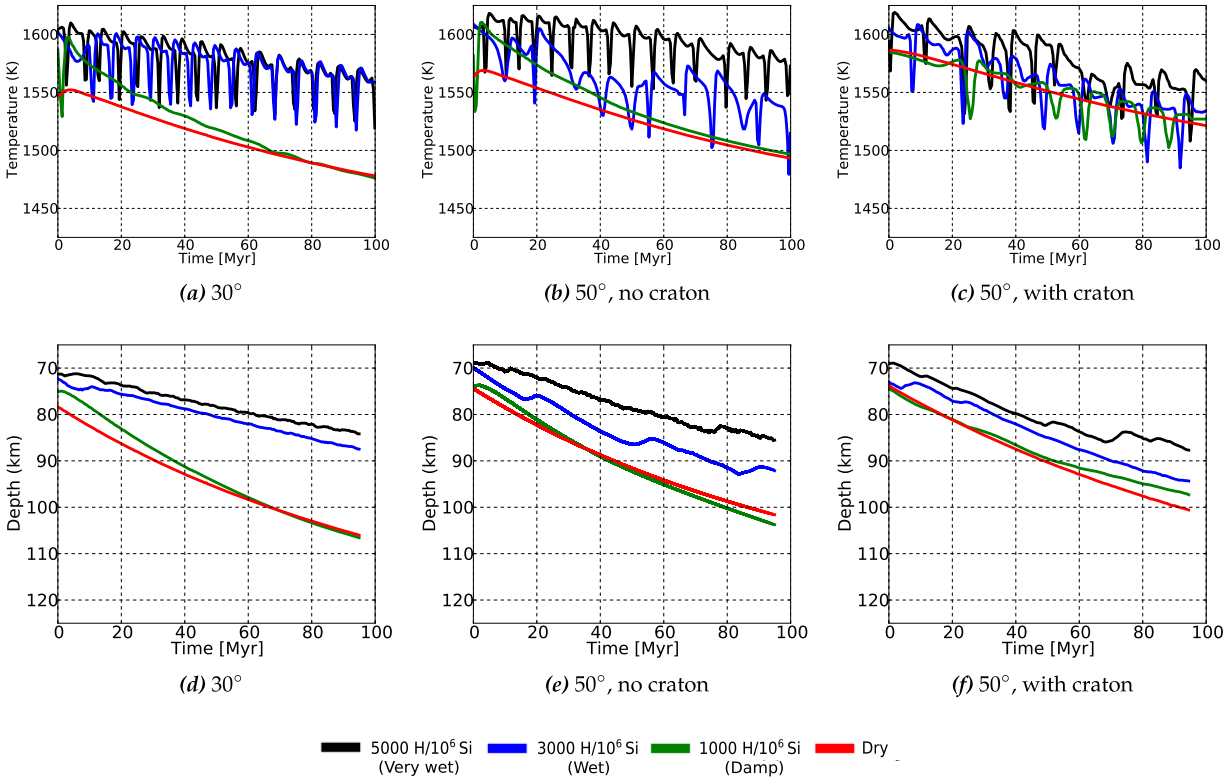

Figure 8. Thermal evolution of the sublithospheric area, labeled "$PROBE_T$" in Figure 1, for models with 50 Myr old upper plates, subduction velocities of 5 cm/yr and a range of water contents: (a) model with a dip angle of 30°; (b) 50°-dipping case, previously presented in Figure 7e; (c) variant of the model in Figure 8b, with a strong lithospheric block/craton, on the right-hand side of the domain. (d–f) illustration of the temporal evolution of the 1400 K isotherm's depth, which we use as a proxy for lithospheric thickness, for these models.

such models will necessarily differ in other respects (e.g., depth extent of the models or boundary conditions at the bottom boundary, which would also affect wedge flow). Nonetheless, the key role of upper-plate length is apparent and this is further highlighted in the following sections.

4.2. Lithospheric Steps

[41] On Earth, back-arc lithosphere is often nonuniform and may contain steps in thickness [e.g., at the continent-ocean boundary, between tectonic and stable continental block boundaries, or as a result of differential hydration, *Arcay et al.*, 2006; *Currie et al.*, 2008]. Such lithospheric steps are well-known nucleation points for instabilities, giving rise to a style of SSC commonly known as edge-driven convection [e.g., *King and Anderson*, 1998; *Hardebol et al.*, 2012]. To examine the role of such instabilities, we include a thicker and stronger block at the top right-hand corner of the domain, with dimensions of 200 km × 200 km, and a fixed viscosity of 10^{24} Pa s, in a model with a 50 Myr old upper plate, a subduction velocity of 5 cm/yr and a dip of 50°. The influence of such a block on instability timescales and lithospheric thickening is illustrated in Figures 8c–8f. We observe two key differences from previous models:

[42] 1. The edge of the lithospheric block allows regular nucleation of instabilities for the damp case, which was marginally stable for models without such a block (cf. Figures 8b and 8c). As a consequence, lithospheric thickness decreases for the damp case, when a craton is present (cf. Figures 8e and 8f).

[43] 2. As demonstrated in section 4.1, conductive lithospheric thickening is enhanced in cases with longer upper plates, and the time interval between gravitational instabilities is more regular. When a stable, fixed craton is introduced (in a model where the domain size remains fixed), the length of lithosphere that is able to destabilize decreases and, accordingly, the time interval between instabilities becomes more irregular. For wet and very wet cases, the lithosphere was sufficiently unstable

in the absence of the craton—the addition of a strong cratonic block, therefore, does not enhance instability. Rather, the additional space constraints lead to slightly increased time intervals between instabilities, in both cases, and a minor increase in lithospheric thickness.

[44] The net effect of a step in lithospheric thickness, therefore, is strongly dependent upon the subduction setting. Nonetheless, in cases that are marginally stable, a step in lithospheric thickness may play an important role in triggering SSC.

4.3. Wedge-Corner Hydration

[45] Investigations into the stability fields of hydrous phases indicate that slab dehydration is limited to a depth of about 200 km [e.g., *Schmidt and Poli*, 1998]. While it remains unclear how water is transported through the wedge, several proposed mechanisms lead to a relatively vertical migration from the point where it is released [e.g., *Gerya and Yuen*, 2003; *Gerya et al*., 2006; *Gorczyk et al*., 2007; *Zhu et al*., 2009]. The consequence of such fluid migration would be that significant hydration is limited to the wedge corner, as was modeled by *Arcay et al*. [2005, 2006], *Cagnioncle et al*. [2007], and *Hebert et al*. [2009], and as was assumed by *Honda and Saito* [2003], *Manea and Gurnis* [2007], *Currie et al*. [2008], and *Honda et al*. [2010].

[46] Hydration localized to the wedge corner introduces a step in strength of the upper plate, which would facilitate instability nucleation. However, at the same time, limiting hydration to the wedge corner limits the region over which instabilities can form. To quantify the net effect of such localized hydration, we have examined several cases where the horizontal extent of the hydrated corner is varied, in addition to the difference in water content between the corner and back-arc region. We find that if the back arc is dry or damp, no drips form for hydrated corners that extend 100 km, or less, from the slab-upper-plate decoupling point: in such a small region the wavelength of a Rayleigh-Taylor instability exceeds the length of the water-weakened upper plate. In our reference models (i.e., those described in section 3), the minimum wavelength of instabilities, in cases with strong hydration throughout the wedge, was 120–150 km. As such, when the hydrated corner extends 150 km from the decoupling point, drips form when the back arc is dry and the corner is very wet. However, they do not form if the corner is wet, or if the back arc is damp. For a hydrated corner extending 200 km horizontally from the decoupling point (i.e., the slab-wedge interface at 80 km depth), instabilities do form for the smaller viscosity contrast between a wet or very wet corner, and a damp back arc. The chief reason that SSC occurs in the very wet corner/dry back-arc case, for the 150 km extent hydrated corner, is the strong viscosity contrast, which provides a nucleation point for instabilities. In addition, for the high-viscosity dry rheology, corner flow is most efficient at eroding the lithosphere over the wedge tip, thus keeping the wedge corner warm enough for instabilities to form.

[47] Thus, if only part of the mantle wedge is significantly hydrated, SSC may only ensue under favorable conditions, where lithospheric destabilization is encouraged by hydration to at least 150 km from the wedge corner (corresponding to a slab depth of 200 km for a 50° dip case), and is aided by high plate velocities, which allow corner flow to keep the wedge corner relatively hot. Previous studies that found SSC in models where only the wedge corner was hydrated assumed a dry back-arc mantle and strong water-weakening in the wedge corner. As in these models, our simulations also show that the lithospheric instabilities mainly nucleate at the dehydration boundary, and lead to enhanced thinning of the hydrated lithosphere, when compared to the damp/dry lithosphere.

5. Implications for Wedge Thermal Structure

[48] Small-scale convection affects upper-plate structure, slab dehydration conditions, the wedge's thermal structure, and the extent and mode of melting [*Arcay et al*., 2005, 2006, 2007; *Currie et al*., 2008]. Each of these are next discussed.

5.1. Upper-Plate Evolution

[49] Thinning of the upper plate beneath the volcanic-arc exerts an important control on the scale and location of the melt zone, the mode of melting, and the depth of mineral dehydration at and above the slab's surface. Lithospheric thinning beneath the back-arc facilitates the localization of deformation, including the formation of back-arc spreading centers, and back-arc melting.

5.1.1. Fore-Arc Lithosphere

[50] Previous studies have documented that kinematically driven wedge-flow models develop

enhanced erosion, or "pinching," of the upper plate beneath the fore arc, when coupling between upper and lower plates is prescribed to a given depth [e.g., *Conder*, 2005; *Arcay et al*., 2005, 2007]. Our dry models are consistent with these previous studies, with: (i) a clear pinch zone developing beneath the fore arc and extending as shallow as our minimum coupling depth of 80 km; and (ii) pinching enhanced in models with higher subduction velocities. For some of our damp cases, mild pinching is observed, which introduces a strong gradient in lithospheric thickness beneath the fore arc, from which instabilities can nucleate. For wet and very wet cases, the pinch zone is poorly developed, as the lithosphere generally does not thicken far beyond 80 km in this cases, due to SSC. We note that in published models with a dynamic slab and rheologically controlled coupling, lithospheric erosion in the fore-arc region is enhanced relative to our models [*Arcay et al*., 2005, 2007].

5.1.2. Back-Arc Lithosphere

[51] A number of observations indicate that several back-arc regions, not recently subjected to extension, have a relatively thin lithosphere ($\approx$ 60 km), over distances of 200–900 km from the trench. These observations include: (i) high back-arc surface heat flow (>70 mW m^{-2} for continental crust with radiogenic heat production; >60 mW m^{-2} for oceanic crust); (ii) low seismic velocities at 50–100 km depth; (iii) temperature estimates from mantle xenoliths; and (iv) widespread sporadic volcanism [*Currie and Hyndman*, 2006]. Most available measurements are for continental back arcs, but include a few oceanic regions [e.g., *Currie and Hyndman*, 2006; *Manga et al*., 2012]. Zones of active back-arc extension also regularly exhibit very slow mantle velocities, up to relatively shallow depths [e.g., *Currie and Hyndman*, 2006; *Wiens et al*., 2008]. *Currie and Hyndman* [2006] proposed SSC at the base of hydrated lithosphere as a mechanism for lithospheric thinning and, subsequently, demonstrated that this can lead to rapid and substantial thinning of a hydrated visco-plastic plate [*Currie et al*., 2008].

[52] In our models with a composite dislocation-diffusion creep rheology, thinning is less strong and rapid: in our wet and very wet cases that exhibit SSC, upper-plate thicknesses of around 70 km are observed at a thermal age of 60 Myr, and around 85 km after 100 Myr, which are slightly greater than the thicknesses of 60 km inferred by *Currie and Hyndman* [2006]. Nonetheless, the lithosphere in our wet and very wet cases can be 20 km thinner (after 100 million years of cooling) than in the dry, corner-flow cases, implying that SSC has a significant influence on upper-plate evolution. We note that our lithospheric thicknesses are greater than those inferred by *Currie and Hyndman* [2006], although all of our models have relatively high plate ages (cooling ages are 55 Myr, or older). Studies of SSC beneath oceanic lithosphere indicate that younger plates have not acquired sufficient negative buoyancy to destabilize [*Davaille and Jaupart*, 1994; *van Hunen et al*., 2003], whilst continental lithosphere is commonly older than oceanic lithosphere and, hence, would be expected to be thicker than 55 Myr old oceanic lithosphere. We find that thinning is most efficient when a large section of the upper plate is hydrated: given that the largest distances of thin, hot back arcs correspond to zones that have experienced significant trench retreat (e.g., Aleutians, Kamchatka), this may suggest that dehydration by melt extraction is less efficient than wedge hydration by the downgoing plate, at least when trench retreat occurs rapidly.

5.2. Slab-Surface Temperatures

[53] The rate at which a slab is heated during subduction controls the depths where hydrous minerals destabilize and, therefore, release their fluids into the overlying wedge [e.g., *Peacock*, 1990a; *Peacock and Wang*, 1999; *Poli and Schmidt*, 2002]. In Figure 9, we show examples of model geotherms at the slab's surface alongside dehydration boundaries for oceanic crust [*Hacker*, 2008] and the stability fields for hydrous mantle minerals [*Grove et al*., 2009].

[54] Below 80 km depth (i.e., the upper-lower plate decoupling depth), slab-surface temperatures (SSTs) can vary by almost 100 K between different cases. We find that higher subduction velocities, higher wedge viscosities, and older upper plates all result in decreased SSTs, which is consistent with recent studies by *Lee and King* [2009] and *Syracuse et al*. [2010]. As such, the completion of dehydration for MORB material at the slab's surface (taken as the boundary where water content drops below 0.1 wt %) can shift by 5–25 km, between the different models examined. It is important to note that in addition to controlling crustal dehydration, SSTs can also affect the dehydration of mantle minerals [e.g., *Peacock*, 1990b, 1996; *van Keken et al*., 2011], where they are exposed at the slab's surface (e.g., in oceanic core complexes). Indeed, if mantle

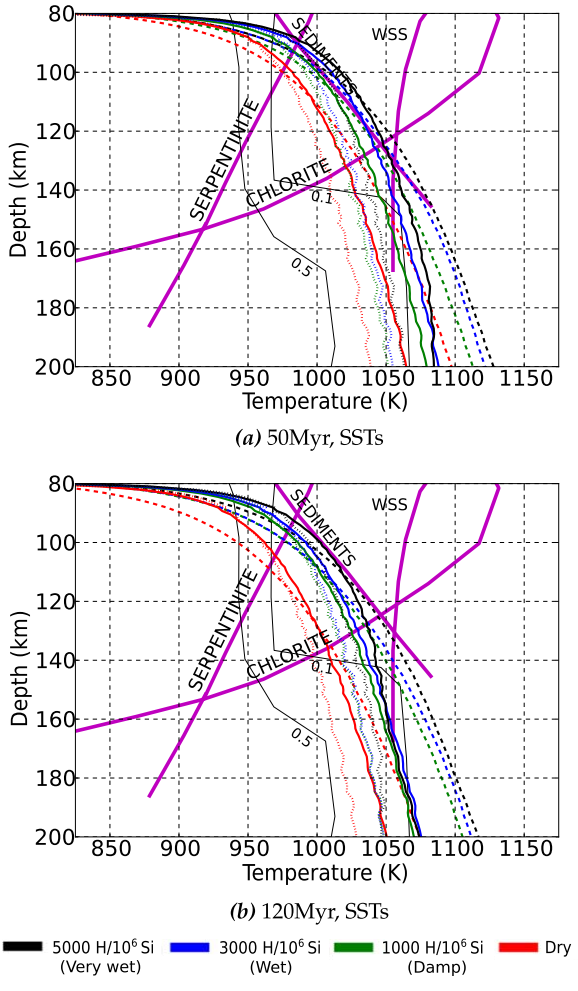

Figure 9. Slab-surface temperatures (SSTs) for a number of models. Dotted, continuous, and dashed lines represent models with subduction velocities of 10, 5, and 2 cm/yr, respectively, with: (a) a 50 Myr old upper plate; and (b) a 120 Myr old upper plate, at a simulation time of 30 Myr. Thin solid black lines are dehydration boundaries (in wt%) for an oceanic crustal composition [*Hacker*, 2008]. The solid magenta lines denote the water-saturated peridotite solidus (labeled WSS), the water-saturated solidus for sediment, and the margins of chlorite and serpentinite stability fields [*Grove et al*., 2012].

minerals are exposed, the range of predicted model SSTs could shift the depth where serpentinite and chlorite breakdown by as much as 25 km.

[55] Temperatures within the slab's mantle lithosphere and, hence, the dehydration of mantle minerals below the oceanic crust, are principally dictated by subduction velocities rather than wedge dynamics [*Syracuse et al*., 2010]. As such, they are not examined here. However, temperatures within the thermal boundary layer above the slab are strongly affected by wedge dynamics. In this thermal boundary layer, hydrous mantle minerals take up water released from the slab until temperatures exceed their stability and fluids are released to migrate through the wedge core or form hydrous melts [e.g., *Grove et al*., 2012]. The thermal boundary layer will further be affected by 50–100 K fluctuations in temperature that are caused by drips from the upper plate, which can be entrained with the flow above the subducting plate (e.g., Figure 4a). We note that in our models, the temperature fluctuations associated with instabilities do not significantly affect the slab surface (aside from the general cooling trend, we see no evidence for transients in our SSTs over time). Conversely, in models by *Arcay et al*. [2005], where more extreme thinning of the upper plate occurs in the arc region, drips are strong enough to result in significant time-dependent cooling of the slab surface.

5.3. Wedge-Core Temperatures and Melting

[56] If a constant viscosity is assumed, analytical scaling relations for mantle wedge temperatures predict that the maximum temperature in the wedge corner scales with the dimensionless quantity: $v_s r\delta^2/\kappa$, where v_s, r, δ, and κ denote subducting slab velocity, distance from the wedge corner, slab dip, and thermal diffusivity, respectively [*England and Wilkins*, 2004]. In general, our composite viscosity models are consistent with this relationship: wedge-corner temperatures tend to increase with subduction velocity, due to enhanced lithospheric thinning and pinching of the upper plate, whilst increasing slab dip allows more warm mantle material into the wedge corner. However, as demonstrated herein, the hydrated rheology modifies the flow regime substantially and, accordingly, exerts a stronger control on wedge temperatures than the basic kinematic parameters of slab dip and subduction velocity. Furthermore, under such a hydrated rheology, SSC induces temperature fluctuations of 50–100 K, on timescales of a few million years. It is therefore important to analyze how such variations in the flow regime, and transient fluctuations in temperature, influence the location, extent and mode of melting within the mantle wedge.

[57] Regions of our models where pressure and temperature conditions exceed the wet and damp solidi of *Katz et al*. [2003] are illustrated in Figure 10. We include only figures for dry, damp, and wet cases, as the melt regions for wet and very wet

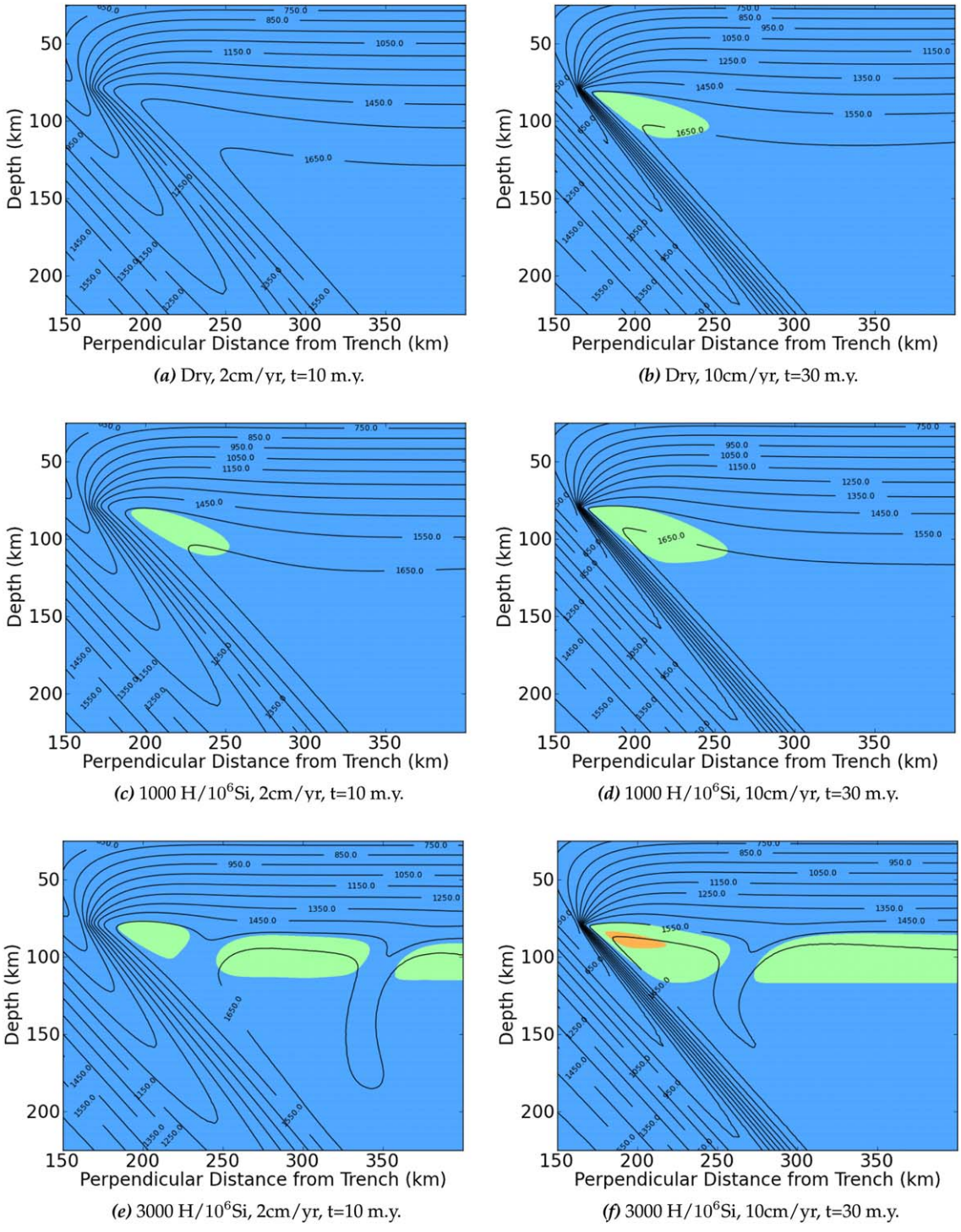

Figure 10. Snapshots of the thermal structure close to the wedge corner for cases with a dry, damp, and wet rheology, at fast and slow subduction velocities. Regions of the wedge where pressure and temperature conditions exceed the wet and damp solidi of *Katz et al*. [2003], for a MORB-source composition, are colored in green and orange, respectively. Snapshots are taken when the original 50 Myr old upper plate has cooled for the same time, t_{cool} = 35 Myr, in both fast and slow cases.

cases are qualitatively very similar. In addition, we draw damp and wet melting contours on all models, as there may be small-scale processes leading to localized high concentrations of fluids that allow for damp/wet melting, but are insufficient to affect the overall rheology [e.g., *Gerya et al*., 2006; *Zhu*

et al., 2011]. This also facilitates comparison between the temperature conditions achieved in different models. Consistent with recent studies by *Grove et al*. [2009] and *England and Katz* [2010], our results demonstrate that melting temperatures are most likely to be exceeded in the wedge corner, below the volcanic-arc region, where high temperature isotherms are drawn up to shallow depths. As a consequence, the region where melting is possible is largest for models with the highest subduction velocities, which exhibit the strongest pinching. In almost all of our models, there is a region, below the volcanic arc, where the wet solidus is exceeded, the exception being the dry, low-velocity case, where the lithosphere is too thick to permit melting (see Figure 10a). In some cases (e.g., the wet case with a subduction velocity of 10 cm/yr—see Figure 10f), there is also a small region where damp melting is possible.

[58] In cases where SSC has thinned the upper plate sufficiently, wet melting is possible beneath the back arc. Whilst the extent of this melt zone is greater for younger upper plates, a thin wet melting region does occur beneath older plates. Significantly, the temperature fluctuations induced by propagating instabilities are sufficient to disrupt melting processes beneath the back arc and volcanic arc (cf. Figures 10e and 10f). *Honda and Yoshida* [2005] proposed SSC to be the cause of time-dependent volcanism in the Japan arc: our models demonstrate that thermal fluctuations, induced by SSC, are sufficient to temporarily shut down the melt supply, on timescales of a few million years (i.e., the time taken for a drip to propagate through the melt zone).

[59] We note that none of the cases examined herein exhibit a thin enough lithosphere beneath the volcanic arc to permit dry melting. Whilst this is consistent with studies by *Grove et al*. [2009] and *Syracuse et al*. [2010], it differs to the predictions of models where shallower coupling depths are imposed [e.g., *England and Katz*, 2010; *Harmon and Blackman*, 2010]. We also note that wedge and slab-surface temperatures would be increased by up to 70 K in our models, had we accounted for the effects of mantle compressibility and viscous dissipation, although this is only a secondary effect [*Lee and King*, 2009].

6. Conclusions and Future Direction

[60] We have undertaken a systematic study into the dominant controls on the flow regime and thermal structure of the mantle wedge, under a range of subduction parameters, considering the influence of buoyancy and a hydrated rheology. Our results demonstrate that under a dry rheology, the flow field exhibits a corner-flow pattern, where the downgoing slab drags sublithospheric material toward the wedge corner and, subsequently, downward parallel to the slab surface, as found in many previous studies [e.g., *Davies and Stevenson*, 1992; *Peacock*, 1996; *Peacock and Wang*, 1999; *van Keken et al*., 2002; *Kelemen et al*., 2003]. However, lower viscosities, which are expected to arise under hydrated conditions ($C_{OH} >= 1000\,H/10^6Si$) [*Karato and Wu*, 1993; *Hirth and Kohlstedt*, 1996], favor the development of SSC, for a wide range of subduction configurations. Although corner flow persists, to some degree, in such cases, instabilities of variable morphologies are initiated at the base of the lithosphere. Their morphology is largely governed by the subduction velocity: in cases with low (2 cm/yr) and intermediate (5 cm/yr) velocities, classical Rayleigh-Taylor type instabilities, or "drips," develop and propagate into the wedge core; conversely, in cases with higher subduction velocities (10 cm/yr), the instabilities take the form of ripples, which are strongly sheared by background mantle flow. Under very wet ($C_{OH} = 5000\,H/10^6Si$) and occasionally under wet ($C_{OH} = 3000\,H/10^6Si$) conditions, the downgoing plate becomes less efficient at driving wedge flow.

[61] There are several indications that back arcs may be wet over large distances. For example, their seismic signatures are often anomalously slow and attenuating, while back-arc lithosphere is regularly observed to be thin [e.g., *Currie and Hyndman*, 2006; *Wiens et al*., 2008; *Hwang et al*., 2011]. Combined with the finger-like seismic structures that are observed in the arc corner below Japan [*Tamura et al*., 2002], which may be the seismic expression of SSC [*Honda and Saito*, 2003], this provides a strong indication that the conditions necessary for SSC are quite often met in natural subduction settings. The link between a hydrated rheology and thin back arcs is confirmed in our models: in wetter cases, SSC reduces lithospheric thickness, with the extent of thinning dominantly controlled by the level of hydration (viscosity) and largely insensitive to subduction velocity. We note, however, that the efficiency of lithospheric thinning is also dependent upon the length of lithosphere that is able to destabilize: if the length of potentially unstable lithosphere is less than the intrinsic wavelength of instabilities

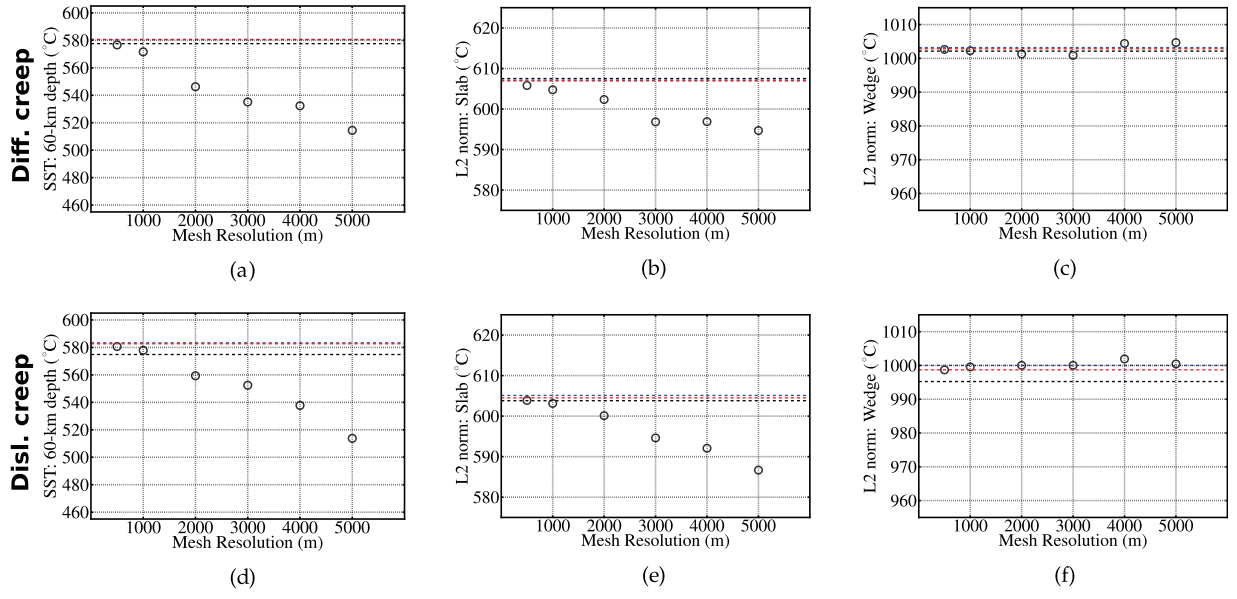

Figure 11. Fluidity's predictions (black circles) of various diagnostics from the benchmark study of *van Keken et al*. [2008]. Dashed horizontal lines denote the highest resolution predictions of three representative codes from the benchmark study: (i) UM (blue); (ii) VT (black); and (iii) PGC (red). Fluidity's results are presented for (a–c) diffusion and (d–f) dislocation creep rheologies, at a range of grid resolutions.

(>100–150 km for our minimum hydrated viscosities of $\sim 1 \times 10^{18}$ Pa s), no SSC develops. Steps or strong gradients in lithospheric strength/thickness, as are observed on Earth, provide nucleation points for instabilities: under such scenarios, the tendency for SSC increases.

[62] In cases where SSC has thinned the upper plate, wet melting is possible beneath the back arc. Furthermore, SSC results in transient pulses of 50–100 K colder, more viscous, material being swept toward the mantle wedge corner. These affect wedge temperatures most strongly in the low-velocity cases, where drips have time to develop fully. Their anomalous temperatures are sufficient to suppress melting and affect the stability of hydrous phases within the thermal boundary layer above the downgoing plate. Different wedge viscosities influence the vigor of wedge convection, such that more hydrated wedges yield overall higher slab-surface temperatures (SSTs). However, in our models, there is no significant time-dependent effect from drips on SSTs.

[63] We note that with a dynamic (temperature and hydration controlled) coupling depth, corner erosion can be stronger, resulting in lower wedge-corner viscosities (due to the presence of high temperature material at lower pressures), increased instability and a stronger influence on slab-surface temperatures [*Arcay et al*., 2006, 2007]. Further complexity may arise from thermo-chemical modes of flow involving low density sediments and melt-fluid mixtures, which can form small-scale, cold plumes that rise from the downgoing plate [*Gerya et al*., 2006; *Zhu et al*., 2009; *Behn et al*., 2011]. The interaction between thermo-chemical plumes and SSC, driven by lithospheric instability, remains to be investigated.

[64] Our results demonstrate that hydrated rheologies promote instabilities in 2-D. Theoretical and numerical studies [e.g., *Richter*, 1973; *Honda and Saito*, 2003; *Wirth and Korenaga*, 2012] predict that in 3-D, longitudinal "Richter" rolls are the dominant form of instability, and that these are enhanced with increasing subduction velocity. This implies that Earth's lithosphere may be even more unstable than we have inferred herein. The flow regimes developing in a hydrated 3-D mantle wedge, and their impacts on mantle wedge thermal structure, therefore, will be subject to a future study. The insights gained through this 2-D investigation will aid in interpreting the 3-D results.

Appendix A: Validating Fluidity Against Benchmark Solutions

[65] Fluidity's accuracy for kinematically driven simulations of mantle wedge flow is demonstrated here via comparisons with the well-established benchmark

of *van Keken et al*. [2008]. The benchmark geometry is the same for all cases: the domain is chosen to be 660 km wide and 600 km deep. It is filled with an incompressible Stokes fluid and split into three regions: (i) a 45°-dipping slab, descending at 5 cm/yr; (ii) a 50 km thick rigid (zero velocity) overriding plate; and (iii) the mantle wedge, where corner flow is induced through viscous coupling with the slab (buoyancy forces are neglected). The inflow boundaries (at both wedge and trench sides) and top of the model have prescribed temperature boundary conditions. Mechanical boundary conditions for the wedge are no-slip below the overriding plate and constant velocity along the top of the slab, with stress free conditions at the wedge boundary. All five model configurations of *van Keken et al*. [2008] (i.e., models with a range of boundary conditions and rheological relations) have been examined. However, for conciseness, we present results only for the most complex cases (2a/2b), which utilize Newtonian temperature dependent diffusion creep and non-Newtonian strain rate dependent dislocation creep rheologies, respectively (thus most closely approximating the models presented herein).

[66] We examine simulations at resolutions ranging from 500 m to 5 km and calculate the same steady state diagnostics as *van Keken et al*. [2008]: (i) the temperature at a single, fixed point on the slab-wedge interface, at coordinates of (60, 60) km; (ii) the discrete *L*2 norm of the slab-wedge interface temperature, between 0 and 210 km depth; and (iii) the discrete *L*2 norm of temperature for the wedge corner, in the 54–120 km depth range. Our results are presented in Figure 11, illustrating the excellent agreement between Fluidity and other numerical codes [e.g., *King et al*., 1990; *van Keken et al*., 2002]: results converge toward the benchmark solutions with increasing resolution, as expected. As such, fluidity can be considered accurate for simulating the class of subduction models that are examined herein.

Acknowledgments

[67] G.L.V. was partially supported by a Janet Watson scholarship from the Department of Earth Science and Engineering at Imperial College. D.R.D. was funded by a Fellowship from NERC (NE/H015329/1). C.R.W. was supported by the National Science Foundation MARGINS program grants OCE-0841079 and EAR-1141976. Numerical simulations were undertaken at: (i) the Imperial College High Performance Computing (ICT-HPC) center; and (ii) HECToR, the UK's national high-performance computing service, which is provided by UoE HPCx Ltd. at the University of Edinburgh, Cray Inc., and NAG Ltd., and funded by the Office of Science and Technology through EPSRC's High End Computing Program. Authors would like to acknowledge support from the Applied Modeling and Computation Group (AMCG) at Imperial College (IC) London. Authors also benefited from discussion with Matthew Piggott (IC), Gareth Collins (IC) and Huw Davies (Cardiff University). Jeroen van Hunen and Saturo Honda are thanked for their thorough and constructive reviews, which helped to improve this manuscript substantially, while Thorsten Becker is acknowledged for efficient and constructive editorial input.

References

Abers, G. A., P. E. van Keken, E. A. Kneller, A. Ferris, and J. C. Stachnik (2006), The thermal structure of subduction zones constrained by seismic imaging: Implications for slab dehydration and wedge flow, *Earth Planet. Sci. Lett.*, *241*, 387–397, doi:10.1016/j.epsl.2005.11.055.

Andrews, D. J., and N. H. Sleep (1974), Numerical modelling of tectonic flow behind island arcs, *Geophys. J. Int.*, *38*(2), 237–251, doi:10.1111/j.1365-246X.1974.tb04118.x.

Arcay, D., M. P. Doin, and E. Tric (2005), Numerical simulations of subduction zones: Effect of slab dehydration on the mantle wedge dynamics, *Phys. Earth Planet. Inter.*, *149*, 133–153, doi:10.1016/j.pepi.2004.08.020.

Arcay, D., M. P. Doin, E. Tric, R. Bousquet, and C. de Capitani (2006), Overriding plate thinning in subduction zones: Localized convection induced by slab dehydration, *Geochem. Geophys. Geosyst.*, *7*, Q02007, doi:10.1029/2005GC001061.

Arcay, D., E. Tric, and M. P. Doin (2007), Slab surface temperature in subduction zones: Influence of the interplate decoupling depth and upper plate thinning process, *Earth Planet. Sci. Lett.*, *255*, 324–338, doi:10.1016/j.epsl.2006.12.027.

Arcay, D., S. Lallemand, and M. P. Doin (2008), Back-arc strain in subduction zones: Statistical observations versus numerical modeling, *Geochem. Geophys. Geosyst.*, *9*, Q05015, doi:10.1029/2007GC001875.

Behn, M. D., P. B. Kelemen, G. Hirth, B. R. Hacker, and H.-J. Massonne (2011), Diapirs as the source of the sediment signature in arc lavas, *Nat. Geosci.*, *4*, 641–646.

Billen, M. I., and M. Gurnis (2001), A low viscosity wedge in subduction zones, *Earth Planet. Sci. Lett.*, *193*(1–2), 227–236, doi:10.1016/S0012-821X(01)00482-4.

Cagnioncle, A. M., E. M. Parmentier, and L. T. Elkins-Tanton (2007), Effect of solid flow above a subducting slab on water distribution and melting at convergent plate boundaries, *J. Geophys. Res.*, *112*, B09402, doi:10.1029/2007JB004934.

Conder, J. A. (2005), A case for hot slab surface temperatures in numerical viscous flow models of subduction zones with an improved fault zone parameterization, *Phys. Earth Planet. Inter.*, *149*(1–2), 1–6, doi:10.1016/j.pepi.2004.08.018.

Currie, C. A., and R. D. Hyndman (2006), The thermal structure of subduction zone back arcs, *J. Geophys. Res.*, *111*, B08404, doi:10.1029/2005JB004024.

Currie, C. A., R. S. Huismans, and C. Beaumont (2008), Thinning of continental backarc lithosphere by flow-induced gravitational instability, *Earth Planet. Sci. Lett.*, *269*, 436–447, doi:10.1016/j.epsl.2008.02.037.

Davaille, A., and C. Jaupart (1994), Onset of thermal convection in fluids with temperature-dependent viscosity: Application to the oceanic mantle, *J. Geophys. Res.*, *99*, 19,853–19,866, doi:10.1029/94JB01405.

Davies, D. R., J. H. Davies, O. Hassan, K. Morgan, and P. Nithiarasu (2008), Adaptive finite element methods in geodynamics—Convection dominated mid-ocean ridge and subduction zone simulations, *Int. J. Numer. Method. H.*, *18*(7–8), 1015–1035, doi:10.1108/09615530810899079.

Davies, D. R., C. R. Wilson, and S. C. Kramer (2011), Fluidity: A fully unstructured anisotropic adaptive mesh computational modeling framework for geodynamics, *Geochem. Geophys. Geosyst.*, *12*, Q06001, doi:10.1029/2011GC003551.

Davies, J. H., and D. J. Stevenson (1992), Physical model of source region of subduction zone volcanics, *J. Geophys. Res.*, *97*, 2037–2070, doi:10.1029/91JB02571.

England, P., and R. F. Katz (2010), Melting above the anhydrous solidus controls the location of volcanic arcs, *Nature*, *467*, 700–704, doi:10.1038/nature09417.

England, P., and C. Wilkins (2004), A simple analytical approximation to the temperature structure in subduction zones, *Geophys. J. Int.*, *159*, 1138–1154, doi:10.1111/j.1365-246X.2004.02419.x.

England, P., R. Engdahl, and W. Thatcher (2004), Systematic variation in the depths of slabs beneath arc volcanoes, *Geophys. J. Int.*, *156*, 377–408, doi:10.1111/j.1365-246X.2003.02132.x.

Furukawa, Y., and S. Uyeda (1989), Thermal state under the Tohoko arc with consideration of crustal heat-generation, *Tectonophysics*, *164*(2–4), 175–187.

Gerya, T. V., and D. A. Yuen (2003), Rayleigh-Taylor instabilities from hydration and melting propel 'cold plumes' at subduction zones, *Earth Planet. Sci. Lett.*, *212*, 47–62, doi:10.1016/S0012–821X(03)00265-6.

Gerya, T. V., J. A. D. Connolly, D. A. Yuen, W. Gorczyk, and A. M. Capel (2006), Seismic implications of mantle wedge plumes, *Phys. Earth Planet. Inter.*, *156*, 59–74, doi:10.1016/j.pepi.2006.02.005.

Gorczyk, W., T. V. Gerya, J. A. D. Connolly, and D. A. Yuen (2007), Growth and mixing dynamics of mantle wedge plumes, *Geology*, *35*(7), 587–590, doi:10.1130/G23485A.1.

Grove, T. L., C. B. Till, E. Lev, N. Chatterjee, and E. Medard (2009), Kinematic variables and water transport control the formation and location of arc volcanoes, *Nature*, *459*, 694–697, doi:10.1038/nature08044.

Grove, T. L., C. B. Till, and M. J. Krawczynski (2012), The role of H20 in subduction zone magmatism, *Annu. Rev. Earth Planet. Sci.*, *40*, 413–439, doi:10.1146/annurev-earth-042711–105310.

Hacker, B. R. (2008), H_2O subduction beyond arcs, *Geochem. Geophys. Geosyst.*, *9*, Q03001, doi:10.1029/2007GC001707.

Hacker, B. R., and G. A. Abers (2004), Subduction factory 3: An excel worksheet and macro for calculating the densities, seismic wave speeds, and H_2O contents of minerals and rocks at pressure and temperature, *Geochem. Geophys. Geosyst.*, *5*, Q01005, doi:10.1029/2003GC000614.

Hardebol, N. J., R. N. Pysklywec, and R. Stephenson (2012), Small-scale convection at a continental back-arc to craton transition: Application to the southern Canadian Cordillera, *J. Geophys. Res.*, *117*, B01408, doi:10.1029/2011JB008431.

Harmon, N., and D. K. Blackman (2010), Effects of plate boundary geometry and kinematics on mantle melting beneath the back-arc spreading centers along the Lau Basin, *Earth Planet. Sci. Lett.*, *298*, 334–346, doi:10.1016/j.epsl.2010.08.004.

Hasenclever, J., J. P. Morgan, M. Hort, and L. H. Rüpke (2011), 2D and 3D numerical models on compositionally buoyant diapirs in the mantle wedge, *Earth Planet. Sci. Lett.*, *311*, 53–68, doi:10.1016/j.epsl.2011.08.043.

Hawkesworth, C. J., B. Dhuime, A. B. Pietranik, P. A. Cawood, A. I. S. Kemp, and C. D. Storey (2010), The generation and evolution of the continental crust, *J. Geol. Soc.*, *167*, 229–248, doi:10.1144/0016-76492009-072.

Hebert, L. B., and M. Gurnis (2010), Geophysical implications of Izu-Bonin mantle wedge hydration from chemical geodynamic modelling, *Isl. Arc*, *19*, 134–150.

Hebert, L. B., P. Antoshechkina, P. Asimow, and M. Gurnis (2009), Emergence of a low-viscosity channel in subduction zones through the coupling of mantle flow and thermodynamics, *Earth Planet. Sci. Lett.*, *278*(3), 243–256, doi:10.1016/j.epsl.2008.12.013.

Hirth, G., and D. Kohlstedt (2003), Rheology of the upper mantle and mantle wedge: A view from the experimentalists, in Inside the Subduction Factory, Geophys. Monogr., vol. *138*, edited by J. Eiler, AGU, Washington, D. C., doi:10.1029/138GM06.

Hirth, G., and D. L. Kohlstedt (1996), Water in the oceanic upper mantle: Implications for rheology, melt extraction and the evolution of the lithosphere, *Earth Planet. Sci. Lett.*, *144*(1–2), 93–108, doi:10.1016/OO12-821X(96)00154-9.

Honda, S. (1985), Thermal structure beneath Tohoku, Northeast Japan—A case study for understanding the detailed thermal structure of the subduction zone, *Tectonophysics*, *112*, 69–102.

Honda, S., and M. Saito (2003), Small-scale convection under the back-arc occurring in the low viscosity wedge, *Earth Planet. Sci. Lett.*, *216*, 703–715, doi:10.1016/S0012-821X(03)00537-5.

Honda, S., and T. Yoshida (2005), Application of the model of small-scale convection under the island arc to the NE Honshu subduction zone, *Geochem. Geophys. Geosyst.*, *6*, Q01002, doi:10.1029/2004GC000785.

Honda, S., T. Gerya, and G. Zhu (2010), A simple three-dimensional model of thermo-chemical convection in the mantle wedge, *Earth Planet. Sci. Lett.*, *290*, 311–318, doi:10.1016/j.epsl.2009.12.027.

Huang, J., S. Zhong, and J. van Hunen (2003), Controls on sublithospheric small-scale convection, *J. Geophys. Res.*, *108*(B8), 2405, doi:10.1029/2003JB002456.

Hwang, Y. K., J. Ritsema, and S. Goes (2011), Global variation of body-wave attenuation in the upper mantle from teleseismic P wave and S wave spectra, *Geophys. Res. Lett.*, *38*, L08311, doi:10.1029/2011GL046812.

Jadamec, M. A., and M. I. Billen (2010), Reconciling surface plate motions with rapid three-dimensional mantle flow around a slab edge, *Nature*, *465*, 338–341, doi:10.1038/nature09053.

Karato, S. (2003), Mapping water content in the upper mantle, in Inside the Subduction Factory, Geophys. Monogr., vol. *138*, edited by J. Eiler, pp. 135–152, AGU, Washington, D. C., doi:10.1029/138GM08.

Karato, S., and P. Wu (1993), Rheology of the upper mantle: A synthesis, *Science*, *260*, 771–778.

Katz, R. F., M. Spiegelman, and C. H. Langmuir (2003), A new parameterization of hydrous mantle melting, *Geochem. Geophys. Geosyst.*, *4*(9), 1073, doi:10.1029/2002GC000433.

Kelemen, P. B., J. L. Rilling, E. M. Parmentier, L. Mehl, and B. R. Hacker (2003), Thermal structure due to solid-state flow in the mantle wedge beneath arcs, in Inside the Subduction Factory, Geophys. Monogr., vol. *138*, edited by J. Eiler, pp. 293–311, AGU, Washington, D. C., doi:10.1029/138GM13.

Kincaid, C., and I. S. Sacks (1997), Thermal and dynamical evolution of the upper mantle in subduction zones, *J. Geophys. Res.*, *102*, 12,295-12,315.

King, S. D., and D. L. Anderson (1998), Edge-driven convection, *Earth Planet. Sci. Lett.*, *160*, 289–296.

King, S. D., A. Raefsky, and B. H. Hager (1990), Conman—Vectorizing a finite-element code for incompressible 2-D convection in the Earth's mantle, *Phys. Earth Planet. Int.*, *59*, 195–207.

Kneller, E. A., P. E. van Keken, I. Katayama, and S. Karato (2007), Stress, strain, and b-type olivine fabric in the fore-arc mantle: Sensitivity tests using high-resolution steady-state subduction zone models, *J. Geophys. Res.*, *112*, B04406, doi:10.1029/2006JB004544.

Kramer, S. C., C. R. Wilson, and D. R. Davies (2012), An implicit free surface algorithm for geodynamical simulations, *Phys. Earth Planet. Inter.*, *194–195*, 25–37, doi:10.1016/j.pepi.2012.01.001.

Lallemand, S., A. Heuret, and D. Boutelier (2005), On the relationships between slab dip, back-arc stress, upper plate absolute motion, and crustal nature in subduction zones, *Geochem. Geophys. Geosyst.*, *6*, Q09006, doi:10.1029/2005GC000917.

Lee, C., and S. D. King (2009), Effect of mantle compressibility on the thermal and flow structures of the subduction zones, *Geochem. Geophys. Geosyst.*, *10*, Q01006, doi:10.1029/2008GC002151.

Long, M. D., and T. W. Becker (2010), Mantle dynamics and seismic anisotropy, *Earth Planet. Sci. Lett.*, *297*, 341–354, doi:10.1016/j.epsl.2010.06.036.

Manea, V., and M. Gurnis (2007), Subduction zone evolution and low viscosity wedges and channels, *Earth Planet. Sci. Lett.*, *264*, 22–45, doi:10.1016/j.epsl.2007.08.030.

Manga, M., et al. (2012), Heat flow in the Lesser Antilles island arc and adjacent back-arc Grenada basin, *Geochem. Geophys. Geosyst.*, *13*, Q08007, doi:10.1029/2012GC004260.

Manning, C. E. (2004), The chemistry of subduction-zone fluids, *Earth Planet. Sci. Lett.*, *223*, 1–16, doi:10.1016/j.epsl.2004.04.030.

McCulloch, M. T., and V. C. Bennett (1994), Progressive growth of the Earth's continental crust and depleted mantle: Geochemical constraints, *Geochim. Cosmochim. Acta*, *58*, 4717–4738, doi:10.1016/0016-7037(94)90203-8.

Peacock, S. M. (1990a), Fluid processes in subduction zones, *Science*, *248*(4953), 329–337, doi:10.1126/science.248.4953.329.

Peacock, S. M. (1990b), Numerical simulation of metamorphic pressure-temperature paths and fluid production in subducting slabs, *Tectonics*, *9*, 1197–1211, doi:10.1029/TC009i005p01197.

Peacock, S. M. (1996), Thermal and petrologic structure of subduction zones, in *Subduction Top to Bottom, Geophys. Monogr.*, vol. *96*, edited by G. E. Bebout, pp. 119–133, AGU, Washington, D. C., doi:10.1029/GM096p0119.

Peacock, S. M., and K. Wang (1999), Seismic consequences of warm versus cool subduction metamorphism: Examples from Southwest and Northeast Japan, *Science*, *286*, 937–939, doi:10.1126/science.286.5441.937.

Plank, T., L. B. Cooper, and C. E. Manning (2009), Emerging geothermometers for estimating slab surface temperatures, *Nature Geosci.*, *2*, 611–615, doi:10.1038/ngeo614.

Poli, S., and M. W. Schmidt (2002), Petrology of subducted slabs, *Annu. Rev. Earth Planet. Sci.*, *30*, 207–235, doi:10.1146/annurev.earth.30.091201.140550.

Richter, F. M. (1973), Convection and the large-scale circulation of the mantle, *J. Geophys. Res.*, *78*, 8735–8745, doi:10.1029/JB078i035p08735.

Rychert, C., F. K. M., G. A. Abers, T. Plank, E. M. Syracuse, J. M. Protti, V. Gonzalez, and W. Strauch (2008), Strong along-arc variation in attenuation in the mantle wedge beneath Costa Rica and Nicaragua, *Geochem. Geophys. Geosyst.*, *9*, Q10S10, doi:10.1029/2008GC002040.

Schmidt, M. W., and S. Poli (1998), Experimentally based water budgets for dehydrating slabs and consequences for arc magma generation, *Earth Planet. Sci. Lett.*, *163*, 361–379.

Seton, M., R. D. Müller, S. Zahirovic, C. Gaina, T. H. Torsvik, G. Shephard, A. Talsma, M. Gurnis, and M. Turner (2012), Global continental and ocean basin reconstructions since 200 Ma, *Earth Sci. Rev.*, *113*, 212–270, doi:10.1016/j.earscirev.2012.03.002.

Syracuse, E. M., and G. A. Abers (2006), Global compilation of variations in slab depth beneath arc volcanoes and implications, *Geochem. Geophys. Geosyst.*, *7*, Q05017, doi:10.1029/2005GC001045.

Syracuse, E. M., P. E. van Keken, and G. A. Abers (2010), The global range of subduction zone thermal models, *Phys. Earth Planet. Inter.*, *183*, 73–90, doi:10.1016/j.pepi.2010.02.004.

Tamura, Y., Y. Tatsumi, D. Zhao, Y. Kido, and H. Shukuno (2002), Hot fingers in the mantle wedge: New insights into magma genesis in subduction zones, *Earth Planet. Sci. Lett.*, *197*, 105–116.

Tatsumi, Y. (1989), Migration of fluid phases and genesis of basalt magmas in subduction zones, *J. Geophys. Res.*, *94*, 4687–4707, doi:10.1029/JB094iB04p04697.

van Hunen, J., J. Huang, and S. Zhong (2003), The effect of shearing on the onset and vigor of small-scale convection in a Newtonian rheology, *Geophys. Res. Lett.*, *30*(19), 1991, doi:10.1029/2003GL018101.

van Keken, P. E. (2003), The structure and dynamics of the mantle wedge, *Earth Planet. Sci. Lett.*, *215*, 323–338, doi:10.1016/S0012-821X(03)00460-6.

van Keken, P. E., B. Kiefer, and S. M. Peacock (2002), High-resolution models of subduction zones: Implications for mineral dehydration reactions and the transport of water into the deep mantle, *Geochem. Geophys. Geosyst.*, *3*(10), 1056, doi:10.1029/2001GC000256.

van Keken, P. E., et al. (2008), A community benchmark for subduction zone modeling, *Phys. Earth Planet. Inter.*, *171*(1–4), 187–197, doi:10.1016/j.pepi.2008.04.015.

van Keken, P. E., B. R. Hacker, E. M. Syracuse, and G. A. Abers (2011), Subduction factory 4: Depth-dependent flux of H_2O from slabs worldwide, *J. Geophys. Res.*, *116*, B01401, doi:10.1029/2010JB007922.

Wada, I., and K. Wang (2009), Common depth of slab-mantle decoupling: Reconciling diversity and uniformity of subduction zones, *Geochem. Geophys. Geosyst.*, *10*, Q10009, doi:10.1029/2009GC002570.

Wiens, D. A., J. A. Conder, and U. Faul (2008), The seismic structure and dynamics of the mantle wedge, *Annu. Rev. Earth Planet. Sci.*, *36*, 421–455.

Wirth, E. A., and J. Korenaga (2012), Small-scale convection in the subduction zone mantle wedge, *Earth Planet. Sci. Lett.*, *357–358*, 111–118, doi:10.1029/2012JB009524.

Zhu, G., T. V. Gerya, D. A. Yuen, S. Honda, T. Yoshida, and J. A. D. Connolly (2009), Three-dimensional dynamics of hydrous thermal-chemical plumes in oceanic subduction zones, *Geochem. Geophys. Geosyst.*, *10*, Q11006, doi:10.1029/2009GC002625.

Zhu, G., T. V. Gerya, S. Honda, P. J. Tackley, and D. A. Yuen (2011), Influences of the buoyancy of partially molten rock on 3-D plume patterns and melt productivity above retreating slabs, *Phys. Earth Planet. Inter.*, *185*, 112–121, doi:10.1016/j.pepi.2011.02.005.